



**Modeling instantaneous dynamic triggering in a 3D fault system:  
application to the June 2000 South Iceland seismic sequence**

Journal:	<i>Geophysical Journal International</i>
Manuscript ID:	draft
Manuscript Type:	Research Paper
Date Submitted by the Author:	n/a
Complete List of Authors:	Bizzarri, Andrea; Istituto Nazionale di Geofisica e Vulcanologia, Sezione di Bologna Belardinelli, Maria; University of Bologna, Physics Department; University of Bologna, Physics Department
Keywords:	Fault interaction, Stress triggering, Earthquake dynamics, Constitutive laws, Numerical models

1  
2  
3  
4  
5  
6  
7  
8  
9  
10  
11  
12  
13  
14  
15  
16  
17  
18  
19  
20  
21  
22  
23  
24  
25  
26  
27  
28  
29  
30  
31  
32  
33  
34  
35  
36  
37  
38  
39  
40  
41  
42  
43  
44  
45  
46  
47  
48  
49  
50  
51  
52  
53  
54  
55  
56  
57  
58  
59  
60

**Modeling instantaneous dynamic triggering  
in a 3–D fault system:  
application to the June 2000 South Iceland seismic sequence**

**A. Bizzarri<sup>1</sup>, M. E. Belardinelli<sup>2</sup>**

<sup>1</sup> Istituto Nazionale di Geofisica e Vulcanologia,

Sezione di Bologna, Bologna, Italy

<sup>2</sup> Università degli Studi di Bologna,

Dipartimento di Fisica, Bologna, Italy

*Paper submitted to Geophysical Journal International*

**October 3, 2007**

*Dynamic triggering in 3–D***Abstract**

We present a model of seismogenesis on an extended 3–D fault subjected to the external perturbations of coseismic stress changes due to an earthquake occurred on another fault (the causative fault). As an application, we consider the spatio–temporal stress distribution produced by the  $M_S = 6.6$  June 17, 2000 mainshock in the South Iceland Seismic Zone (SISZ) on the Hvalhnúkur fault. The latter is located nearly 64 km from the causative fault and failed 26 s after the mainshock with an estimated magnitude  $M_w \in [5, 5.5]$ , providing an example of instantaneous dynamic triggering. The stress perturbations are computed by means of a discrete wavenumber and reflectivity code. The response of the perturbed fault is then analyzed solving the *truly* 3–D, fully dynamic (or spontaneous) problem, accounting for crustal stratification. In a previous study, the response of the Hvalhnúkur fault was analyzed by using a spring–slider fault model, comparing the estimated perturbed failure time with the observed origin time. In addition to the perturbed failure time, the present model can provide numerical estimates of many other dynamical features of the triggered event that can be compared with available observations: the rupture history of the whole fault plane, its final extension and the seismic moment of the 26 s event. We show the key differences existing between a mass–spring model and the present extended fault model, in particular we show the essential role of the load exerted by the other slipping points of the fault. By considering both rate– and state–dependent laws and non–linear slip–dependent law, we show how the dynamics of the 26 s fault strongly depends on the assumed constitutive law and initial stress conditions. In the case of rate– and state– dependent governing laws, assuming an initial effective normal stress distribution which is suitable for the SISZ and consistent with previously stated conditions of instantaneous dynamic triggering of the Hvalhnúkur fault, we obtain results in general agreement with observations.

**Key words:** Fault interaction, stress triggering, earthquake dynamics, constitutive laws,

numerical models.

## 1. Introduction

Earthquake slip results in a stress redistribution with respect to the initial state of the seismogenic area: a net local shear stress decrease on the fault surface (stress drop) and a variation of the stress tensor components in the surrounding medium caused by the propagation of seismic waves. In particular, stress increase can cause further earthquakes or aftershocks.

In spite of the logical and apparent simplicity of the above-mentioned mechanism, fault triggering is not a well understood phenomenon. First of all it has not been observed as widely as expected (King et al., 1994). Moreover, impeding understanding of this mechanism, there is a general ignorance about the initial state of fault(s) — in term of pre-stress, fault surface geometry and segmentation, initial sliding velocity etc. — and several uncertainties about the physical processes occurring during faulting such as the analytical form of the governing law describing them.

In this paper we will focus on the so-called instantaneous (or immediate) dynamic triggering, i. e. a kind of dynamic triggering that is realized soon after the arrival of the seismic waves of the causative event in the location of the triggered one (e.g. Belardinelli et al., 2003; Ziv et al., 2006). The triggering effect considered in this work occurs in a temporal interval of tens of seconds and in a spatial distance of several tens of kilometers from the causative event.

Remote triggering is a case of dynamic triggering occurring at distances larger than the dimension of the causative fault. Since the  $M_w$  7.7 1992 Landers earthquake only a few examples of remote triggering of earthquakes have been observed:  $M_w$  7.1 1999 Hector Mine EQ (Gomberg et al., 2001),  $M_s$  7.6 1988 Gulf of Alaska EQ,  $M_s$  7.1 1989 Loma Prieta EQ (Stark and Davis, 1996),  $M_w$  7.4 1999 Izmit EQ (Brodsky et al., 2000) and  $M_w$  7.9 2002 Denali EQ (Eberhart-Phillips et al., 2003). The early events in Reykjanes Peninsula of the June 17, 2000 seismic sequence in the South

*Dynamic triggering in 3-D*

Iceland Seismic Zone (SISZ hereinafter) fail in this small class of examples.

This seismic sequence took place in the SISZ and in the Reykjanes Peninsula (RP in the following) starting in June 2000 (see Figure 1). It was very well monitored by different local networks: strong motion network, volumetric strain meter networks, digital seismic stations and permanent GPS stations (Arnadottir et al., 2000, 2001, 2004). We recall here only some features of this sequence, as all the details are given in a previous paper (Antonioli et al., 2006; AEA06 in the following) and references therein. The sequence started on June 17, at 15:40:41 UTC (this corrects a misprint in AEA06), with an event of magnitude  $M_s = 6.6$  (Pedersen et al., 2001), with hypocenter located at the absolute coordinates of (63.973 °N, 20.367 °W, 6.3 Km) (Stefansson et al., 2003; Arnadottir et al., 2006). Three early events occurred along the SISZ and its prolongation along the RP at 8 s ( $M_l = 3.5$ ), 26 s ( $M_l = 5.5$ ) and 30 s ( $M_l = 5.5$ ) after the June 17 mainshock, respectively. The 26 s and 30 s events are associated to the arrival of the shear waves of the mainshock (Vogfjord, 2003).

Conditions to have instantaneous dynamic triggering of these three events were found by AEA06 using a simple 1-D spring-slider analog model of perturbed fault and comparing the modeled failure times with the observed origin ones. Of these three events, the 26 s event is the best constrained from seismological observations and therefore in the following of this study we will focus on this aftershock, which occurred on the Hvalhnúkur fault (H in Figure 1). Its hypocenter is located at (63.951 °N, 21.689 °W, 8.9 Km); latitude and longitude have uncertainties of 0.004° and 0.008°, respectively. The hypocenter depth uncertainty is 1.3 km, allowing us to consider the possible a focal depth up to 7.6 Km (Vogfjord, 2003, personal communication). The Hvalhnúkur fault is here assumed as a north-south, vertical, right-lateral fault as in AEA06 and Arnadottir et al. (2004).

The main goals of the present paper can be summarized as follows:

- i) To study the instantaneous remote triggering of one of the early events of the June 2000 seismic sequence in SISZ, by means of a realistic 3-D fault model, including heterogeneities in

the crustal profile and in the fault rheology;

- ii) To characterize the initial stress on the fault of the early event here studied, by comparing the available observations with the 3–D model estimates of hypocenter location, rupture extension and seismic moment, besides the model failure time. In the light of this fact, we extend the conclusions of AEA06;
- iii) To study the dependence of the response of the triggered fault on the assumed constitutive relation: rate– and state–dependent laws and slip–dependent law.

## 2. The numerical approach

### 2.1. Basic ingredients

First of all we compute the stress field variations due to the June 17 mainshock using the discrete wavenumber and reflectivity code developed by Cotton and Coutant (1997) and assuming exactly the same set of parameters and the same ramp source time function

$(f(t) = \frac{1}{2} \left[ 1 + \tanh\left(\frac{t}{t_0}\right) \right])$ ; Bouchon, 1981, with  $t_0 = 1.6$  s) used in AEA06. We neglected the stress

perturbations due to the 8 s aftershock owing to the large distance from the 26 s event (see Figure 1) and the smaller magnitude with respect to the mainshock. The crustal profile corresponds to the east of Hengill structure (continuous line in Figure 2 of AEA06; see also Vogfjord et al., 2002). The values of the perturbation stress tensor are calculated on the 26 s fault plane up to 2.78 Hz, in a total of  $12 \times 8$  “receivers”, located in nodes uniformly spaced 1650 m in the strike direction and at depths of 0 m, 1650 m, 3300 m, 4950 m, 6550 m, 8100 m, 9900 m and 11550 m. The coordinates of the receivers are expressed in a Cartesian coordinate system  $OX_1X_2X_3$ , having the origin  $O$  on the free surface at the epicenter of the June 17 mainshock (see Figure 2a). In the local coordinate system  $Ox_1x_2x_3$  the plane  $\Sigma$  (Figure 2b), defined by  $x_2 = x_2^f = 5$  km, represents the 26 s fault and the nominal location of its hypocenter is (16500,5000,8900) m.

### *Dynamic triggering in 3–D*

The computed values of the stress perturbations are interpolated in space and also in time to correctly resolve the dynamic processes occurring on the 26 s fault, according to the findings of Bizzarri and Cocco (2003) and Bizzarri and Cocco (2005; BC05 thereafter). In the following we will indicate with  $\Delta\sigma_{2i}(x_1, x_3, t)$ , or more briefly with  $\Delta\sigma_{2i}$  ( $i = 1, 2, 3$ ), the results of this spatio–temporal interpolation, which is described in Appendix A.

Finally, these interpolated perturbations are included in the equations of motion representing the fully dynamic, spontaneous (i. e. without prior imposed rupture velocity) rupture problem, solved by using the *truly* 3–D (i. e. not mixed–mode), finite difference code presented in BC05 (details are summarized in Appendix B).

#### **2.2. The response of the extended fault**

In the following of the paper a fault point is considered to fail if the modulus of its slip velocity is greater than, or equal to, a threshold value  $v_p$ , assumed to be equal to 0.1 m/s, in agreement with Belardinelli et al. (2003), Rubin and Ampuero (2005) and AEA06. The instant of time at which this occurs is denoted with the symbol  $t_p$ , the perturbed rupture (or failure) time. The first fault point where the condition  $v \geq v_p$  is satisfied (i. e. where the minimum non zero value of the array  $t_p(x_1, x_3)$  is realized) defines what we call “virtual” hypocenter (indicated with the symbol H henceforth); the adjective is motivated by the fact that this point is obtained as a part of the numerical solution.

We would emphasize that the present model of an extended fault provides several additional details of the triggered event, with respect to a spring–slider analog model of fault. In AEA06, due to the point–like approximation in the modelling of triggering, only the perturbed failure time in the observed hypocenter was given. Here we can estimate the rupture history and the slip distribution on the whole fault of the triggered event. On the other hand, the present model requires a more complex parameterization of the fault surface state than spring–slider model. The latter is built upon a physical model of pore fluid pressure suitable for the SISZ and upon the comparison of synthetic

solutions and other observational constraints on the extended rupture of the triggered event, reported in Appendix C.

### 3. Results with the Dieterich–Ruina law

Among the different possibilities proposed in tribology (see for instance Ohnaka, 2003; Bizzarri and Cocco, 2005, 2006c), we assume for now that the Hvalhnúkur fault is governed by the Dieterich–Ruina (DR thereafter) rate– and state–dependent law (Linker and Dieterich, 1992; AEA06; Bizzarri and Cocco, 2006a, 2006b), which expresses the frictional resistance  $\tau$  as

$$\tau = \mu(v, \Psi) \sigma_n^{eff} = \left[ \mu_* + a \ln\left(\frac{v}{v_*}\right) + b \ln\left(\frac{\Psi v_*}{L}\right) \right] \sigma_n^{eff} \quad (2)$$

$$\frac{d}{dt} \Psi = 1 - \frac{\Psi v}{L} - \left( \frac{\alpha_{LD} \Psi}{b \sigma_n^{eff}} \right) \frac{d}{dt} \sigma_n^{eff}$$

In (2)  $\mu$  is the friction coefficient,  $\mu_*$  and  $v_*$  are reference parameters;  $a$ ,  $b$  and  $\alpha_{LD}$  are the constitutive parameters;  $v$  is the modulus of the fault slip velocity (namely the time derivative of the displacement discontinuity, that is:  $v \equiv \sqrt{v_1^2 + v_3^2}$ ).  $\Psi$  is the state variable, accounting for previous slip episodes,  $L$  is a scale length and  $\sigma_n^{eff}$  is the effective normal stress expressed by (B.3). The values of the constitutive parameters used in this paper, if not otherwise mentioned, are listed in Table 1. In all cases presented in Sections 3 to 5 we assume, as in AEA06, that at  $t = 0$  the fault is in steady state conditions, i. e.  $(d/dt) \Psi = 0$  in equations (2).

#### 3.1. A simple test case

To explain remote instantaneous triggering on the Hvalhnúkur fault with the DR law, one of the



### Dynamic triggering in 3-D

conclusions of AEA06 was that the parameter  $A = a\sigma_n^{eff}$ , characterizing the direct effect on friction, has to be small enough. Consequently, due to the possible values of  $a$ , a very small value of the effective normal stress (or equivalently a near-lithostatic pore fluid pressure) at the hypocentral depth of the 26 s event is required.

We firstly verified that if pore fluid pressure is hydrostatic at every depth, no triggering occurs also in the present extended fault model. In a subsequent test case (case A in Table 2), we chose the most simple configuration (even if physically unrealistic), in which the initial effective normal stress is everywhere equal to  $\sigma_n^{eff*} = 2.5$  MPa, as estimated by AEA06 in the hypocenter of the studied event. The resulting rupture times are reported in Figure 3 from which we can see that the model rupture reaches the surface despite of the observational constraints (Appendix C.1). In fact, the magnitude of the event, the depth of the hypocenter, the absence of geodetic coseismic signals and surface effects (Clifton et al., 2003, Arnadottir et al., 2004) and the aftershock distribution (Hjaltadottir and Vogfjord, 2005) suggest that the seismic rupture of the 26 s events is confined below several km depth. From Table 2 we can see that in case A the vertical extent of the rupture area is overestimated, as well as the seismic moment which is calculated as explained in Appendix C.1. In the following of the paper we will therefore illustrate other test cases performed in order to find if assuming a more realistic initial effective normal stress profile, it is possible to better reproduce observations.

### 3.2. Experiments with spatially variable initial normal stress

We introduce an initial effective normal stress ( $\sigma_n^{eff}$ ) which varies with depth, as physically reasonable for the seismogenic region here considered (Zencher et al., 2006). The pore fluid pressure is assumed to be hydrostatic below the depth  $x_3^* = 5800$  m, and near-lithostatic for  $x_3 \geq x_3^* + D^* = 8800$  m (Figure 4a). The choice of these depth values is discussed and justified in Appendix C.2.

1  
2  
3  
4 A first attempt to model  $\sigma_{n_0}^{eff}$  is profile #1 (dashed grey line in Figure 4b), where we assume a  
5  
6  
7 near–lithostatic pore pressure for  $x_3 > x_3^*$  (dashed grey line in Figure 4a). With this profile we  
8  
9  
10 inhibit the rupture propagation at shallow depth ( $x_3 < x_3^*$ ). This is a consequence of the increase of  
11  
12  
13  $\sigma_n^{eff}$  with decreasing depth, which in turn causes the parameter  $A$  to increase. However, with profile  
14  
15  
16 #1 we overestimate the total seismic moment ( $M_0 = 1.94 \times 10^{17}$  Nm). A second attempt is  
17  
18  
19 represented by profile #2 (dotted grey line in Figure 4b) where the transition from hydrostatic to  
20  
21  
22 near–lithostatic pore pressure values is linear over the region of width  $x_3^* \leq x_3 < x_3^* + D^*$  (transition  
23  
24  
25 region, dotted grey line in Figure 4a), as corroborated by the model of Zencher et al. (2006). In this  
26  
27  
28 case, we cannot obtain nucleation at all since the threshold value  $v_l$  is never attained on the fault.

29  
30 Finally we consider profile #3 (continuous grey line in Figure 4b) in which with the single  
31  
32  
33 parameter  $h^*$  it is possible to span the range between the extreme cases of profile #1 and profile #2  
34  
35  
36 (see equation (C.2)). In this profile the pore pressure increases exponentially to near–lithostatic  
37  
38  
39 values with increasing depth in the transition region (continuous grey line in Figure 4a). The results  
40  
41  
42 obtained with this profile for  $h^* = 360$  m are reported in Figure 5 (case B in Table 2). The least value  
43  
44  
45 of the perturbed failure time is slightly lower than the observed origin time, but, as a consequence  
46  
47  
48 of the hydrostatic pore fluid pressure values at shallow depth, the vertical rupture extension now  
49  
50  
51 agrees with observations: it does not propagate above a depth of 6400 m, which is one kilometer  
52  
53  
54 below the limit inferred from aftershocks distributions (see Appendix C.1). For this synthetic event  
55  
56  
57 the total seismic moment estimate is  $M_0 = 6.43 \times 10^{16}$  Nm, which corresponds to a moment–  
58  
59  
60 magnitude  $M_w = 5.21$ , in the range of observations.

Looking at the time snapshots of the slip velocity on the fault plane (Figures 5b, 5c and 5d) we  
can see a pulse propagating towards the free surface and expanding in the strike direction. Below  
the depth of 7500 m the fault slip velocity remains well below  $v_l$ .

*Dynamic triggering in 3-D***3.3. Heterogeneous rheology**

In order to reproduce the confinement of the Hvalhnúkur rupture along the strike direction that can be roughly envisaged by the aftershock distribution (region  $\mathcal{A}$  defined in Appendix C.1) we have assumed a velocity strengthening rheology (i. e.  $a > b$ ;  $a = 0.012$ ) for  $x_1 < 9700$  m and  $x_1 > 16500$  m. These regions are associated with aseismic behaviour and they act like barriers (see Bizzarri et al., 2001).

The resulting rupture times of this case C are shown in Figure 6 (summarized in Table 2): the coordinates of H, its failure time and the extension along the dip of the rupture are identical to those obtained in the previous, fully homogeneous case B, that is, the fault evolution in H is unaffected by the presence of the lateral velocity strengthening areas. However, now the seismic rupture is confined in the velocity weakening region  $9700 \text{ m} \leq x_1 \leq 16500 \text{ m}$ , as expected by the imposition of artificial barriers. Consequently, the seismic moment is now  $M_0 = 2.27 \times 10^{16} \text{ Nm}$  ( $M_w = 4.90$ ), which is smaller than the lower bound of the acceptable range (see Appendix C.1). All these informations tend to suggest that the *ad hoc*-imposed lateral rheological heterogeneities do not significantly improve the results of numerical model.

**4. Comparison with spring–slider results**

In this section we focus our attention on the temporal evolution of dynamic variables in the location (target point) of H for the previously discussed case B. In Figure 7 results of the present extended fault (3-D model; black solid squares) are compared with those obtained with a spring–slider analog model of fault (SS model; grey open circles). In the SS numerical experiment we introduce the same stress perturbations acting in the target point of the 3-D simulation. The comparison is made assuming the same constitutive parameters and governing law.

Looking at Figure 7a we can see that the solutions of the 3-D and SS fault models agree in the

1  
2  
3  
4 first part of the simulation, for very low values of slip velocity. This confirms that the quasi-static  
5 approximation used in the SS simulation is adequate for low values of slip velocity. We emphasize  
6 again that in all 3-D numerical experiments presented in this paper the system is fully dynamic in  
7 the whole range of variability of fault slip velocity. The agreement between the two solutions is  
8 good until the time  $t_A = 24.10$  s (light grey dashed line in Figures 7a, 7b and 7d), corresponding to  
9 the largest peak of the shear stress perturbation ( $-\Delta\sigma_{21}$  in the present notation) and to the beginning  
10 of the acceleration phase in the 3-D model (Figure 7b). For  $t > t_A$  the two solutions become  
11 different: the 3-D system accelerates up to final instability ( $t_p = 24.94$  s, full vertical line in Figures  
12 7a, 7b and 7d), while in the SS model the slip velocity remains smaller than  $v_l$  and, after a  
13 deceleration phase (ending in the point B in Figure 7a), it slowly increases again with time to  
14 provide a delayed failure of the system at  $t = 3.36$  days (not shown in Figure 7).

15  
16  
17  
18  
19  
20  
21  
22  
23  
24  
25  
26  
27  
28  
29  
30 This different behavior of the two models can be explained considering the different elastic  
31 loads exerted on the two systems. Unlike the SS, the 3-D model in H is also affected by the load  $\mathbf{f}_r$   
32 exerted by the neighboring points, that, even moving with  $v < v_p$  produce shear and normal loads  
33 that at each time level are superimposed on the stress perturbations due to June 17 mainshock (see  
34 Appendix B). This contribution in the strike component of total shear load is clearly visible in  
35 Figure 7d, where we can see that for  $t < t_A$  the shear loads are indistinguishable in the two models,  
36 but just before the peak of the shear stress perturbation, the restoring forces  $\mathbf{f}_r$  begin to become  
37 significant, increasing the peak of the total shear load in the 3-D model (reached at  $t = 24.30$  s  $> t_A$ ).  
38 This peak is high enough to enhance seismic slipping in the 3-D model, unlike the SS model.  
39  
40  
41  
42  
43  
44  
45  
46  
47  
48  
49

50  
51 From the slip-weakening curve (Figure 7c) we can see that the maximum value of traction  
52 ( $\tau_u^{eq}$ ) is the same in both models, as well as the equivalent slip-weakening distance ( $d_0^{eq}$ ) and the  
53 final level of traction ( $\tau_f^{eq}$ ). The two curves differ for slip values smaller than the value reached at  
54 point C in Figure 7c. Actually, in the SS case there is an early partial stress release (first weakening  
55  
56  
57  
58  
59  
60

### Dynamic triggering in 3-D

episode) that occurs at  $t \cong t_A$  when the first peak of slip velocity is realized (Figure 7a).

In the present study, as in the 2-D study made by Bizzarri and Cocco (2003), we can note that the fault point accelerates and exceeds the threshold velocity  $v_l = 0.1$  m/s (i. e. it behaves seismically, grey star in Figure 7d) before the traction reaches its kinetic level, unlike what was stated by Voisin et al. (2004). This is even more evident if we decrease the threshold value of sliding velocity: with  $v_l = 0.05$  m/s the failure point fails in the middle of weakening process and with  $v_l = 0.01$  m/s it is just at the beginning of the breakdown phase (open black stars in Figure 7c).

## 5. Importance of the governing law: the Ruina–Dieterich model

In this section we assume a different evolution equation for the state variable, the so-called slip law (Ruina, 1983) in order to quantify how results are affected by this different governing law. In this constitutive model — referred as RD thereafter — the frictional traction can be written as (Beeler et al., 1994; Bizzarri and Cocco, 2006a, 2006b):

$$\tau = \left[ \mu_* + a \ln\left(\frac{v}{v_*}\right) + b \ln\left(\frac{\Psi v_*}{L}\right) \right] \sigma_n^{eff} \quad (3)$$

$$\frac{d}{dt} \Psi = -\frac{\Psi v}{L} \ln\left(\frac{\Psi v}{L}\right) - \left( \frac{\alpha_{LD} \Psi}{b \sigma_n^{eff}} \right) \frac{d}{dt} \sigma_n^{eff}$$

We adopt the same governing parameters used in simulations presented in sections 3.2 and 3.3 (cases B and C) and therefore the initial conditions are also the same. However, due to the different evolution of  $\Psi$ , for  $t > 0$  the values of the frictional traction  $\tau$  are different.

Results for this configuration (case D) are shown in Figure 8. The rupture has nearly the same extension along strike as in case C because it has been obtained using the same velocity strengthening regions as rheological barriers. In spite of this, compared to case C, the vertical

extension of the rupture is larger and the seismic moment  $M_0 = 2.02 \times 10^{16}$  Nm ( $M_w = 4.87$ ) is smaller, suggesting that the RD law predicts a slightly smaller average fault slip than the DR law.

In the present case we obtain the smallest perturbed failure time,  $t_p = 23.44$  s (black continuous lines in Figures 8b and 8c). Perturbed failure occurs before the time of the peak of the along strike component of the stress perturbation (now  $t_A = 24.03$  s; light grey dashed lines in Figures 8b and 8c), accordingly the time delay  $t_d = t_p - t_A$  is negative:  $t_d = -0.59$  s (Figure 8c). These differences can be explained recalling that the RD law is more unstable than the DR law for the same initial conditions and constitutive parameters (e. g. Belardinelli et al., 2003, Bizzarri and Cocco, 2003). The traction vs. slip curve (Figure 8d) show an equivalent slip–weakening distance nearly 5 mm long: it is therefore smaller than that arising from the DR law, in agreement with Bizzarri and Cocco (2003). Finally, we remark that also in the case of RD law, H accelerates to instability before reaching the final kinetic frictional level (grey star in Figure 8d).

With the RD law we perform the same comparison between the 3–D model and the SS model made in the previous section. Unlike the previous results, using the RD law the SS model also shows instantaneous dynamic triggering. Both the SS and the 3–D models are characterized by negative time delays (see Figure 8c), but the perturbed failure time in the SS model is  $t_p = 23.93$  s, larger than in the 3–D model. We can therefore exclude the possibility that, for the same governing law, constitutive parameters, initial conditions and perturbing stress, a more complex and realistic model of fault can predict a least perturbed failure time larger than the SS estimate. Moreover, it is confirmed that the 3–D model is more unstable than the SS model, due to the different elastic loads, as discussed in the previous section.

## 6. The non–linear slip–weakening friction law

One alternative to the class of rate– and state–dependent governing equations is represented by the slip–dependent laws; here we have considered the following form of the slip–weakening (see for

*Dynamic triggering in 3-D*

instance Ohnaka and Yamashita, 1989):

$$\tau = \left\{ \left[ \left( \frac{\tau_0}{\sigma_n^{eff}} - \mu_f \right) \left( 1 + \alpha_{OY} \ln \left( 1 + \frac{u}{\beta_{OY}} \right) \right) \right] e^{-\frac{u}{d_0}} + \mu_f \right\} \sigma_n^{eff} \quad (4)$$

where  $\alpha_{OY}$  and  $\beta_{OY}$  are constitutive parameters that controls the slip-hardening phase,  $\mu_f$  is the dynamic (or kinetic) value of the friction coefficient and  $u$  is the fault slip. The coupling of fault strength with stress perturbations is again expressed by equations (B.1) and (B.2).

As explained in the Auxiliary material, the governing parameters in (4) are chosen to reproduce the slip-weakening curve previously obtained with DR law (Figure 7c). In this configuration (case E) H is located at (22500,7700) m (see Figure 9a), far from the strike location of the observed hypocenter, and the estimate of the seismic moment is  $M_0 = 2.49 \times 10^{19}$  Nm, much larger than the maximum value suggested by observations. In this case, unlike case B, the initial effective normal stress is actually unable to confine the rupture along the depth within the region  $\mathcal{I}$  suggested by observations (see Appendix C.1) and a slip velocity of several meters per second is attained, even at the free surface (see Figure 9b). On the other hand, imposing a confinement of the rupture by introducing frictional heterogeneities (formally we set a sufficiently high fault strength for  $x_1 < 9700$  m and  $x_1 > 16500$  m and for  $x_3 > x_3^* + D^*$ ) the threshold value  $v_l$  is never attained on the fault.

In principle, we can not exclude that for a specific set of constitutive parameters appearing in equation (4), the fault strength is such that nucleation will occur inside  $\mathcal{I}$  in agreement with the observations, but such a systematic exploration of the parameter domain is certainly beyond the objectives of the present work. We only notice that, unlike the rate- and state-dependent laws, for a set of constitutive parameters giving the same frictional resistance, the non-linear slip-weakening law (even with its initial slip-hardening phase mimicking the direct effect of rate- and state-dependent laws) is not able to reproduce the main physical features of the aftershock considered in



1  
2  
3  
4 this paper.  
5  
6  
7  
8

## 9 10 **7. Discussion and conclusions**

11  
12 In this paper we present results of numerical experiments in which a *truly* 3–D (i. e. not mixed–  
13 mode) fault governed by different constitutive laws is influenced by external stress perturbations  
14 due to a remote earthquake. We focus our attention on the *instantaneous* dynamic triggering  
15 phenomenon (triggering realized after the arrival of the seismic waves propagating from the  
16 causative event with a delay smaller than the wave train duration). This effect, also called  
17 *immediate* or *with no delay*, can explain early events occurring after a mainshock (at times of the  
18 order of the travelling time of the seismic wave generated by the mainshock). Transient stress  
19 perturbations, such as seismic waves at remote distance, are able to produce only instantaneous  
20 triggering effects, according to several models where failure is assumed to be preceded by an  
21 accelerating phase (e.g. Gombert, 2001; Belardinelli et al., 2003). The observational evidences of  
22 early events are scarce compared to delayed aftershocks that are instead widely observed during a  
23 seismic sequence (e.g. Ziv, 2006). This can be due both to the intrinsic difficulty to detect a seismic  
24 event occurring within the wave train packet generated by a previous event, but also to the  
25 peculiarity of regions where these effects were observed and interpreted, mainly volcanic or  
26 geothermal provinces.  
27  
28  
29  
30  
31  
32  
33  
34  
35  
36  
37  
38  
39  
40  
41  
42  
43  
44  
45

46 Using the rate– and state–dependent laws and a spring–slider model of fault, instantaneous  
47 dynamic triggering can be reproduced provided that the perturbed fault is in critical conditions (e.g.  
48 Belardinelli et al., 2003), that is assuming fine tuned values of the model parameters. One of the  
49 main motivations of this paper is to see if it is possible to reproduce this kind of triggering effects  
50 with an extended fault model and adopting different governing laws on the fault.  
51  
52  
53  
54  
55  
56

57 As an application of the model we consider the fault interaction occurred between the June 17,  
58 2000 mainshock in the South Iceland Seismic Zone and the early event that occurred after 26 s on  
59  
60



*Dynamic triggering in 3–D*

1  
2  
3  
4 the Hvalhnúkur fault, which is located at a remote distance from the mainshock (about 64 km).  
5  
6 From a seismological point of view this event is the best constrained among the three early  
7  
8 aftershocks observed within 30 s after the June 17, 2000 mainshock. Moreover, for this event the  
9  
10 interactions with previous seismic events and different from the mainshock can be reasonably  
11  
12 excluded. We aim to remark that our model can be applied to other cases of instantaneous triggering  
13  
14 even if, as in all computational experiments, the value of the parameters of the model have to be  
15  
16 tuned according to the specific event we want to reproduced, assuming that enough observational  
17  
18 knowledge of the event is available.  
19  
20

21  
22 The fundamental elasto–dynamic equation, accounting for the stress perturbations due to the  
23  
24 mainshock, is solved without any approximations in the whole range of fault slip velocity by using  
25  
26 the finite difference code presented in BC05. Both shear and normal components of the stress  
27  
28 perturbation tensor are accounted for (in agreement with the Coulomb failure criterion, largely used  
29  
30 in fault interaction studies), as well as the heterogeneous properties of the elastic medium  
31  
32 surrounding the 26 s fault. The stress perturbations are calculated by using the discrete wavenumber  
33  
34 and reflectivity method on the whole Hvalhnúkur fault plane.  
35  
36

37  
38 The three early aftershocks observed in the SISZ were analyzed in a previous paper (AEA06),  
39  
40 where the conditions to reproduce the origin time of all of them were already stated by means of a  
41  
42 spring–slider model (SS model). The results presented here are new with respect to that paper, as  
43  
44 well as previously published studies of instantaneous dynamic triggering that used a 2–D fault  
45  
46 model (Voisin et al., 2000) to describe the fault response. In fact, only adopting a 3–D fault model it  
47  
48 is possible to obtain as a part of the solution several additional and important details of the  
49  
50 simulated triggered event, such as the rupture history on the whole fault surface and the seismic  
51  
52 moment. These numerical estimates are compared with available observations.  
53  
54

55  
56 Our 3–D modelling of the Hvalhnúkur fault inevitably requires a more detailed  
57  
58 parameterization than previous modelling since the state of the fault should be specified in each  
59  
60 point of its surface. In general we assume the same homogeneous conditions as in AEA06, except

1  
2  
3  
4 for the initial effective normal stress  $\sigma_{n_0}^{eff}$  for which we assume a depth dependence in agreement  
5  
6  
7 with an independent physical model proposed for the SISZ (Zencher et al., 2006) and with the value  
8  
9 estimated by AEA06 at hypocentral depth. In the Zencher et al (2006) model an increase from  
10  
11 hydrostatic to near–lithostatic pore fluid pressure, within the so–called transition zone, is realized at  
12  
13 seismogenic depth (see Figure 4). In the case of the early aftershock here examined this choice was  
14  
15 shown to be efficient both in explaining the nucleation time of the triggered rupture and its limited  
16  
17 vertical extension, suggested by several evidences, avoiding the *ad hoc* introduction of other kinds  
18  
19 of barriers.  
20  
21

22  
23 One important result of the present paper is that we can reproduce dynamic triggering effects (i.  
24  
25 e. induced failure) with a model of an extended fault, regardless the constitutive law. This is not a  
26  
27 trivial results, considering the findings of Belardinelli et al. (2003) who thoroughly described the  
28  
29 extreme difficulty to model dynamic triggering with the rate– and state–dependent laws. Moreover,  
30  
31 for the 26 s early event in the SISZ, we show here that with rate– and state–dependent laws and  
32  
33 profile #3 of Figure 4, we can obtain estimates of the perturbed failure time, vertical extension of  
34  
35 the fault rupture, hypocenter location and the seismic moment in general agreement with the  
36  
37 available observational constraints (cases B to D).  
38  
39

40  
41 The comparison between the two formulations of the rate– and state–dependent laws (case C  
42  
43 and D) confirms previous results (e.g. Belardinelli et al., 2003) showing that the RD law (case D;  
44  
45 Figure 8) is more unstable than the DR law (case C; Figure 6). In particular, the RD law is shown to  
46  
47 provide the smallest perturbed failure time.  
48  
49

50  
51 We have also compared the time evolution of solutions in the “virtual” hypocenter obtained  
52  
53 with a SS model and the present 3–D one. These two fault model are intrinsically different, but both  
54  
55 with the DR law (case B) and with the RD law (case D) we have observed an excellent agreement  
56  
57 during the slow nucleation phase (when the fault slip velocity is of the order of the initial one).  
58  
59 During the subsequent acceleration phase, unlike the SS model, each point of the 3–D model is  
60  
affected not only by the external stress perturbations due to the causative event, but also by the load

*Dynamic triggering in 3-D*

exerted by the neighboring points that are already slipping. This implies that the perturbed failure time estimates of the 3-D model are systematically smaller than that given by the SS model.

Our results clearly show that the least value of the perturbed failure time on the Hvalhnúkur fault slightly underestimates the observed origin time of the 26 s event. Analogous underestimate was previously obtained with a SS model. This discrepancy could be attributed to problems in the estimate of the perturbing stress, related to *i*) the assumed crustal profile and *ii*) the assumed source time function. We analyze this second possibility by recomputing the stress perturbations induced by the June 17 mainshock with a translated and more causal form of the Bouchon source time function ( $f(t) = \frac{1}{2} \left[ 1 + \tanh\left(\frac{t-t_0}{t_0}\right) \right]$ ; Cotton and Campillo, 1995, again with  $t_0 = 1.6$  s). Applying these stress perturbations to a 3-D fault parameterized as in case B, we obtain almost the same spatial feature of the rupture (compare Figures 5a and 10), but a larger estimate of the least perturbed failure time ( $t_p = 26.42$  s; case F in Table 2), which is closer to the observations.

We have also considered (case E in Table 2) a non-linear slip-dependent friction law with an initial hardening stage, as analytically postulated by Ida (1972; his Figure 1). This formulation can be regarded as an alternative to the rate- and state- laws and overcomes the non-physicality of other expressions of the slip-weakening law (Andrews, 1976; Voisin, 2002; Voisin et al., 2004) that predict that a fault point is completely locked before traction reaches the maximum yield stress. Nevertheless, by assuming governing parameters giving the same frictional resistance of the DR case, it is not possible to reproduce the 26 s aftershock rupture. In particular, the effective normal stress is not sufficient to arrest the crack propagation along the depth, unlike the case of rate- and state-dependent laws.

To summarize, the study of the response of an extended 3-D fault to external stress perturbations performed here provides further support to a possible mechanism for the instantaneous dynamic triggering observed in the year 2000 in the SISZ. Our results suggest that the triggered rupture might be confined within the transition zone from near-lithostatic (at depth) to

1  
2  
3  
4 hydrostatic pore fluid pressure values, located just above the brittle–ductile transition depth.  
5  
6  
7

8 **Acknowledgements.** We would like to thank Maurizio Bonafede for providing us material in  
9  
10 advance of publication.  
11  
12  
13  
14  
15  
16  
17  
18  
19  
20  
21  
22  
23  
24  
25  
26  
27  
28  
29  
30  
31  
32  
33  
34  
35  
36  
37  
38  
39  
40  
41  
42  
43  
44  
45  
46  
47  
48  
49  
50  
51  
52  
53  
54  
55  
56  
57  
58  
59  
60

For Peer Review

## Appendix A. Interpolation of the stress perturbation

In order to have a sufficient spatio-temporal resolution for the fully dynamic code we develop an algorithm that employs a  $C^2$  cubic spline, often used in seismological applications (e. g. Ripperger and Mai, 2004) to interpolate the values of the stress perturbation generated by the June 17 mainshock. Quantities  $\Delta\sigma_{2i}(x_1, x_3, t)$  ( $i = 1, 2, 3$ ) in section 2.1 are the results of such an interpolation, described below. The  $C^2$  cubic spline is a smooth and one of the most heavily used fourth-order piecewise polynomial functions, that in general are given by (in the univariate case):

$$p(x) = \sum_{r=1}^k c_{rs} \frac{(x - \xi_s)^{r-1}}{(r-1)!}, \quad \text{for } \xi_s \leq x < \xi_{s+1} \quad (\text{A.1})$$

where  $k$  is the order (degree  $k - 1$ ) of their polynomial pieces,  $\xi \in \mathbb{R}^n$  represents the breakpoint sequence and the  $\{c_{rs}\}$  is the  $k \times (n - 1)$  matrix of their local polynomial coefficients. The breakpoints of the spline are the abscissas, while endpoint conditions are automatically determined by the program. These conditions correspond to the “not-a-knot” condition (see de Boor, 1978), which requires that the third derivative of the spline be continuous at the second and next-to-last breakpoint.

Technically, our algorithm proceeds as follows:

- 1) The original grid of receivers is settled, defining all discrete receivers coordinates on the fault  $(x_{1_l}^{old}, x_{3_m}^{old})$ , for  $l = 1, \dots, l_{end}$ ,  $m = 1, \dots, m_{end}$ . In our specific case are:  $l_{end} = 12$  and  $m_{end} = 8$ ;
- 2) The values of stress perturbations at constant depth (i. e. at constant  $x_3^{old}$  coordinate) are interpolated in the new grid points  $x_{1_i}^{new}$ , giving vectors  $\Delta\sigma_{2j}^{new}(x_{1_i}^{new}, x_{3_m}^{old}, t^{old})$ ,  $i = 1, \dots, i_{end}$ ,  $j = 1, 2, 3$ .

- 1  
2  
3  
4  
5  
6  
7  
8  
9  
10  
11  
12  
13  
14  
15  
16  
17  
18  
19  
20  
21  
22  
23  
24  
25  
26  
27  
28  
29  
30  
31  
32  
33  
34  
35  
36  
37  
38  
39  
40  
41  
42  
43  
44  
45  
46  
47  
48  
49  
50  
51  
52  
53  
54  
55  
56  
57  
58  
59  
60
- 3) Values of stress perturbations at constant  $x_1^{old}$  coordinate are interpolated in the new grid points  $x_{3k}^{new}$ , giving vectors  $\Delta\sigma_{2j}^{new}(x_{1l}^{old}, x_{3k}^{new}, t^{old})$ ,  $k = 1, \dots, k_{end}$ ,  $j = 1, 2, 3$ ;
  - 4) Values of  $\Delta\sigma_{2j}^{new}(x_{1l}^{old}, x_{3k}^{new}, t^{old})$  determined at point 3 are interpolated in each new point  $x_{1i}^{new}$ , giving new vectors  $\Delta\tilde{\sigma}_{2j}^{int(3)}(x_{1i}^{new}, x_{3k}^{new}, t^{old})$ ,  $i = 1, \dots, i_{end}$ ,  $k = 1, \dots, k_{end}$ ,  $j = 1, 2, 3$ ;
  - 5) Values of  $\Delta\sigma_{2j}^{new}(x_{1i}^{new}, x_{3m}^{old}, t^{old})$  determined at point 2 are interpolated in each new point  $x_{3k}^{new}$ , giving new vectors  $\Delta\tilde{\sigma}_{2j}^{int(1)}(x_{1i}^{new}, x_{3k}^{new}, t^{old})$ ,  $i = 1, \dots, i_{end}$ ,  $k = 1, \dots, k_{end}$ ,  $j = 1, 2, 3$ ;
  - 6) The values of the stress perturbations in the new points  $(x_{1i}^{new}, x_{3k}^{new})$  and at each time  $t^{old}$  are simply obtained as the arithmetic average of  $\Delta\tilde{\sigma}_{2j}^{int(1)}$  and  $\Delta\tilde{\sigma}_{2j}^{int(3)}$ :
 
$$\Delta\sigma_{2j} = \frac{1}{2} \left( \Delta\tilde{\sigma}_{2j}^{int(1)} + \Delta\tilde{\sigma}_{2j}^{int(3)} \right), j = 1, 2, 3;$$
  - 7) Points 2 to 6 are iterated for each time levels  $t^{old}$ .

Finally, we have to interpolate in time the spatially interpolated value of the stress perturbations, obtained as described above. Also for the temporal interpolation, we use a  $C^2$  cubic spline to obtain the desired temporal discretization  $\Delta t = 1.27 \times 10^{-3}$  s. This spatio-temporal discretization satisfies the convergence and stability conditions discussed BC05. Considering the adopted crustal profile, their equation (A.4) gives  $173 \text{ m} = \sqrt{3} \Delta x > v_{p_{max}} \Delta t = 8.6 \text{ m}$ . From equations (A.5) of BC05 we have that the critical spatial and temporal sampling are

$$\Delta t^* = \frac{v_{S_{min}} \rho_{min} L}{4\omega_{CFL_{max}} \left( (b-a) \sigma_n^{eff} \right)_{max}} \cong \frac{v_{S_{min}} \rho_{min} L}{4\omega_{CFL_{max}} (b-a) \sigma_n^{eff} (x_1, x_3^*, 0)} = 27.6 \times 10^{-3} \text{ s} \text{ and}$$

$$\Delta x^* = \frac{v_{S_{min}}^2 \rho_{min} L}{4\omega_{CFL_{max}}^2 \left( (b-a) \sigma_n^{eff} \right)_{max}} = 1035 \text{ m}, \text{ respectively (in the latter equation } \omega_{CFL} \text{ is the}$$

*Dynamic triggering in 3-D*

Courant–Friedrichs–Lewy ratio, which is:  $\omega_{CFL} \stackrel{\text{df}}{=} v_s \Delta t / \Delta x$ . In our case  $\omega_{CFL_{max}} = 0.04826$ .

Therefore both the continuum approximation conditions in (A.6) of BC05 are comfortably satisfied.

The discretization used here gives solutions without numerical oscillation due to spatial grid dispersion up to a critical frequency  $f_{acc}^{(s)} = 3.02$  Hz, comparable with the maximum frequency at which stress tensor perturbation are calculated (2.78 Hz). Computational efficiency of the numerical code for the solution of the spontaneous problem does not require an (auto)adaptive method for numerical integration and therefore the temporal discretization can be kept constant over the whole simulation.

In Figure A.1 we plot two time snapshots of the distribution on the 26 s faults of the along strike component of the shear stress perturbation before (panels on the left) and after (panels on the right) the spatio–temporal interpolation previously described. In Figure A.2 we compare in the 26 s hypocenter (black stars in Figure A.1) the time histories of the perturbations. In Figure A.2a we plot the strike component of the shear traction perturbation and in Figure A.2b the normal component. We emphasize that the (original) stress values in the black curves of figure A.2 have been calculated by using the discrete wavenumber and reflectivity code, but these values have not been included in the array of the 96 receivers used for the interpolation. This was to maximize the differences between the original and the new (interpolated) values (red curves in figure A.2) in order to test the reliability of the proposed interpolation algorithm. Looking at Figures A.1 and A.2 we can conclude that all the main features of the stress perturbation field are preserved after the spatio–temporal interpolation and also the local values in the time series are maintained. A small difference appears in the normal component, but it does not affect the results presented and discussed in this paper.

## Appendix B. Solution to the problem of the induced extended rupture

In this paper times are referred to the June 17, 2000 mainshock origin time. At time  $t$ , in each node of the  $x_2 = x_2^f$  fault plane ( $\Sigma$ ), we compute the total loads:

$$\mathcal{L}_i = f_{r_i} + T_{0_i} + \Delta\sigma_{2i} \quad (i = 1 \text{ and } 3). \quad (\text{B.1})$$

In (B.1)  $T_{0_i}$  are the components of the initial shear traction (described below) and  $f_{r_i}$  are the components of the load  $\mathbf{f}_r$  (namely the contribution of the restoring forces per unit fault area) exerted by the neighboring points of the fault. Formally  $f_{r_i} = (M^- f_i^+ - M^+ f_i^-) / (M^+ + M^-)$ , where  $M^+$  and  $M^-$  are the masses of the “+” and “-” half split-node of the fault plane  $\Sigma$  (see Figure 2b);  $\mathbf{f}^+$  represents the force per unit fault area acting on partial node “+” caused by deformation of neighbouring elements located in the “-” side of  $\Sigma$  (and viceversa for  $\mathbf{f}^-$ ).

The stress tensor perturbations  $\{\Delta\sigma_{2i}\}$  are coupled to the components of the fault friction  $T_i$  through the following equations:

$$\begin{aligned} \frac{d^2}{dt^2} u_1 &= \alpha [\mathcal{L}_1 - T_1] \\ \frac{d^2}{dt^2} u_3 &= \alpha [\mathcal{L}_3 - T_3] \end{aligned} \quad (\text{B.2})$$

where  $\alpha \equiv \mathcal{A} ((1/M^+) + (1/M^-))$ ,  $\mathcal{A}$  being the split-node area (in the present vertical fault case is:  $\mathcal{A} = \Delta x_1 \Delta x_3$ ). The boundary condition here imposed is expressed as  $T = \tau$ , where  $T$  is the modulus of the total shear traction  $\mathbf{T}^{(\hat{n})}$  acting on the fault ( $T = \sqrt{T_1^2 + T_3^2}$ , see Figure 2b), and  $\tau$  is the frictional resistance, which depends on the adopted constitutive relation and is proportional to the effective normal traction acting on the fault. The latter is  $\sigma_n^{eff} = -(\boldsymbol{\Sigma}^{(\hat{n})} \cdot \hat{\mathbf{n}} + p_{fluid})$  where  $\boldsymbol{\Sigma}^{(\hat{n})} \cdot \hat{\mathbf{n}}$  is the normal stress acting on the solid matrix and  $p_{fluid}$  is the pore fluid pressure. At time  $t$  the effective normal stress is:



*Dynamic triggering in 3-D*

$$\sigma_n^{eff} = -f_{r_2} + \sigma_{n_0}^{eff} - \Delta\sigma_{22} \quad (\text{B.3})$$

where  $\sigma_{n_0}^{eff}$  is the initial value of the effective normal stress. The components of the shear pre-stress acting on the fault are  $T_{0_1} = \tau_0(x_1, x_3)\cos(\varphi_0)$  and  $T_{0_3} = \tau_0(x_1, x_3)\sin(\varphi_0)$ , where  $\varphi_0 \equiv \varphi(x_1, x_3, 0)$  is the initial azimuth (i.e., the initial rake) and  $\tau_0(x_1, x_3)$  is the initial value of friction resistance prescribed by the fault governing law. Taking into account that for our geometry the unit vector normal to  $\Sigma$  is  $\hat{\mathbf{n}} // \hat{x}_2 \equiv (0, 1, 0)$  and that the shear traction is acting on the positive side of  $\Sigma$ , in the present case of a right-lateral fault  $\varphi_0 = 180^\circ$ . Here, as in the BC05 and Bizzarri and Cocco (2006a, 2006b) normal components of the stress tensor are assumed to be negative for compression; notice that the opposite notation was used in AEA06.

## Appendix C. Parameterization of 26 s fault

### C.1. Fault dimension and seismic moment

The 26 s event produced a small geodetic signal and minor surface effects compared to the 30 s event, suggesting that the rupture area is deep and relatively small (Clifton et al., 2003, Arnadóttir et al., 2004). Relocated aftershocks of the 26 s event are grouped around two depths: about 4.5 km and 8 km (Hjaltadóttir and Vogfjörð, 2005; their Figure 12). According to Boatwright and Cocco (1996), Scholz (2002), De Martini et al. (2004) the aftershocks tend to group in the locations where the main rupture produces a stress concentration, i. e. around the rupture perimeter where the crack tip is arrested or in almost locked regions of the sliding surface. From the aftershock distribution we can therefore consider that the seismic part of the fault extends between the depths  $x_3 = 5400$  m and  $x_3 = 7400$  m; we will indicate this depth interval with the symbol  $\mathcal{I}$ . The aftershock latitudes are between  $63.890^\circ\text{N}$  and  $63.951^\circ\text{N}$  (the latitude of the 26 s hypocenter). This latitude interval corresponds to  $x_1 \in [9700, 16500]$  m in our local Cartesian reference system  $Ox_1x_2x_3$ . A vertical alignment of un-relocated aftershocks is observed only in the north end latitude interval. We then define the region  $\mathcal{A} = \{ \mathbf{x} \mid x_1 \in [9700, 16500] \text{ m}, x_2 = x_2^f, x_3 \in [5400, 7400] \text{ m} \}$  as a possible candidate of the rupture area, even if, on the basis of the aftershock distribution, its horizontal extent is less constrained than the vertical extent ( $\mathcal{I}$ ).

We can estimate the static seismic moment of the 26 s event from the well-known relation  $\text{Log}(M_0) = 1.5M_w + 9$  (Kanamori, 1977). Considering an estimated magnitude  $M_w \cong 5$  (Arnadóttir et al., 2006; Vogfjörð, 2003) we obtain  $M_0$  of the order of  $3.2 \times 10^{16}$  Nm. This value would be increased up to  $1.8 \times 10^{17}$  Nm if a moment-magnitude up to 5.5 is assumed (Arnadóttir et al., 2004; AEA06). We compare the observed value of  $M_0$  with the value of the (dynamic) seismic moment  $M(t)$ , as evaluated at the end of the numerical simulation. The latter is computed as

### Dynamic triggering in 3-D

$M(t) = \frac{|\lambda_1'| + |\lambda_2'|}{2}$ , where  $\lambda_1$  and  $\lambda_2$  are two of the three eigenvectors of the (dynamic) seismic

moment tensor  $\bar{M}(t)$ , ordered such that  $|\lambda_1'| \geq |\lambda_2'| \geq |\lambda_3'|$  (e. g. Dziewonski et al., 1981). For our pure

double couple geometry it is:  $M(t) = \sqrt{M_{21}(t)^2 + M_{23}(t)^2}$ , where

$$M_{2i}(t) = \iint_{\Sigma} G(x_3) u_i(x_1, x_3, t) dx_1 dx_3 ; \quad i = 1, 2 \quad (\text{C.1})$$

where  $G$  is the depth-variable rigidity modulus, and  $u_1$  and  $u_3$  are fault slip components.

### C.2. Initial effective normal stress

The effective normal stress acting at  $t = 0$  on the 26 s fault plane is assumed to vary only with depth ( $\sigma_n^{eff}(x_1, x_3, 0) = \sigma_{n_0}^{eff}(x_3)$ ), since it is evaluated as the difference existing between the lithostatic

pressure  $\hat{p}^{(litho)}(x_3)$ , the deviatoric normal stress of tectonic origin  $\Delta\sigma^{(dev)} = 5.7$  MPa and the pore

fluid pressure  $p_{fluid}(x_3)$ :  $\sigma_{n_0}^{eff}(x_3) = \hat{p}^{(litho)}(x_3) - \Delta\sigma^{(dev)} - p_{fluid}(x_3)$ . The lithostatic pressure was

computed as  $\hat{p}^{(litho)}(x_3) = \hat{\rho}_{rock} g x_3$ ,  $\hat{\rho}_{rock}$  being the weighed averaged cubic mass rock density

(using the relation  $\hat{\rho}_{rock} \equiv \sum_{k=1}^4 \rho_{rock_k} \frac{x_{3k} - x_{3k-1}}{x_{34}}$ , with  $x_{3_0} \equiv 0$ ) and  $g$  the acceleration of gravity.

At shallow depths ( $x_3 \leq x_3^*$ ) the pore fluid pressure is assumed to be hydrostatic,

$p_{fluid}^{(hydro)}(x_3) = g \int_0^{x_3} \rho_{fluid}(x_3') dx_3'$ , where at each depth the fluid density (Table B.1) is calculated

iteratively (assuming constant fluid density in each kilometer) by using a reasonable temperature

profile in Iceland (e. g. Beblo and Bjornsson, 1980; Hersir et al., 1984) and extracting  $\rho_{fluid}(x_3)$

from pressure-temperature tables of Haar et al. (1984). For  $x_3 \geq x_3^* + D^*$  we assume

near-lithostatic pore fluid pressure values  $p_{fluid}^{nl}(x_3)$ , giving  $\sigma_{n_0}^{eff}(x_3) = \sigma_n^{eff*} = 2.5$  MPa, as in

AEA06. We recall here that Hubbert and Rubey (1959) observed that water, provided by

dehydration reactions, can exist at near–lithostatic pressures and consequently shear fracturing can occur at very low shear stress. More recently, the over–pressurized fluids are of particular interest in studies related to oil reservoir partitions (Hunt, 1990; Powley, 1990), as well as to larger–scale crustal processes, such as the reduction of strength of mature faults and the earthquake cycles (Byerlee, 1990, 1993; Rice, 1992; Miller et al., 1996). High values of pore fluid pressure are also suggested by Crampin et al. (2002), who studied the polarization of shear wave splitting data recorded in a seismically active area in northern Iceland.

Accordingly, we assume a transitional region of vertical width  $D^*$  where pore fluid pressure varies from hydrostatic to near–lithostatic values, in agreement with numerical results of Zencher et al. (2006), who model the behavior of pore fluid pressure migrating from a reservoir at lithostatic pressure toward the Earth's surface after the rupture of an impermeable barrier of thickness  $D^*$ . We associate  $x_3^* + D^*$  with the brittle–ductile transition depth, which is around 8 km in the SISZ (Arnadottir et al., 2006; see their Figure 13 with the related discussion and AEA06). On the other hand, we believe that the 26 s rupture developed above the brittle–ductile transition and then within the transitional region. Therefore, looking at the aftershock depth distribution discussed in Appendix C.1, we assume a thickness  $D^* = 3$  km (a reasonable value also proposed by Zencher et al., 2006) and  $x_3^* = 5800$  m. In particular, in the transitional region ( $x_3^* < x_3 < x_3^* + D^*$ ) we consider a pore fluid pressure that increases exponentially and gives the following profile of the initial effective normal stress:

$$\sigma_{n_0}^{\text{eff}} = \sigma_n^{\text{eff}*} \left[ e^{-\frac{x_3 - x_3^*}{h^*}} (\Delta P_2 - 1) + 1 \right] \quad (\text{C.2})$$

where  $\Delta P_2 \equiv \hat{p}^{(\text{litho})}(x_3^*) - \Delta \sigma^{(\text{dev})} - p_{\text{fluid}}^{(\text{hydro})}(x_3^*)$  ( $p_{\text{fluid}}(x_3^*) = 48.02$  MPa is the resulting fluid pressure at  $x_3^* = 5800$  m).

*Dynamic triggering in 3-D***References**

- Andrews, D. J. (1976), Rupture propagation with finite stress in antiplane strain, *J. Geophys. Res.*, *81*, No. 20, 3575–3582.
- Antonioli, A., M. E. Belardinelli, A. Bizzarri, and K. S. Vogfjord (2006), Evidence of instantaneous dynamic triggering during the seismic sequence of year 2000 in South Iceland, *J. Geophys. Res.*, *111*, B03302, doi: 10.1029/2005JB003935.
- Arnadottir, T., H. Geirsson, B. H. Bergsson, and C. Völksen (2000), The Icelandic continuous GPS network – ISGPS, March 18, 1999 – February 20, 2000, Rep. VI-R00002-JA02, 36 pp., Icelandic Meteorol. Off., Reykjavík, Iceland.
- Arnadottir, T., H. Geirsson, and P. Einarsson (2004), Coseismic stress changes and crustal deformation on the Reykjanes Peninsula due to triggered earthquakes on 17 June 2000, *J. Geophys. Res.*, *109*, doi:10.1029/2004JB003130.
- Arnadottir, T., S. Hreinsdottir, G. Gudmundsson, P. Einarsson, M. Heinert, and C. Völksen (2001), Crustal deformation measured by GPS in the south Iceland seismic zone due to two large earthquakes in June 2000, *Geophys. Res. Lett.*, *28*, 4031–4033.
- Arnadottir, T., W. Jiang, K. L. Feigl, H. Geirsson, and E. Sturkell (2006), Kinematic models of plate boundary deformation in southwest Iceland derived from GPS observations, *J. Geophys. Res.*, *111*, B07402, doi: 10.1029/2005JB003907.
- Arnadottir, T., S. Jónsson, R. Pedersen, and G. B. Gudmundsson (2003), Coulomb stress change in the South Iceland Seismic Zone due to two large earthquakes in June 2000, *Geophys. Res. Lett.*, *30*, No. 5, 1205, doi: 10.1029/2002GL016495.
- Beblo, M., and A. Bjornsson (1980), A model of electrical resistivity beneath NE-Iceland, Correlation with temperature, *J. Geophys.*, *47*, 184–190.
- Beeler, N. M., T. E. Tullis, and J. D. Weeks (1994), The roles of time and displacement in the evolution effect in rock friction, *Geophys. Res. Lett.*, *21*, No. 18, 1987–1990.
- Belardinelli, M. E., A. Bizzarri, and M. Cocco (2003), Earthquake triggering by static and dynamic

1  
2  
3  
4  
5  
6  
7  
8  
9  
10  
11  
12  
13  
14  
15  
16  
17  
18  
19  
20  
21  
22  
23  
24  
25  
26  
27  
28  
29  
30  
31  
32  
33  
34  
35  
36  
37  
38  
39  
40  
41  
42  
43  
44  
45  
46  
47  
48  
49  
50  
51  
52  
53  
54  
55  
56  
57  
58  
59  
60

stress changes, *J. Geophys. Res.*, 108, No. B3, 2135, doi: 10.1029/2002JB001779, ESE 1-1-1-16.

Bizzarri, A., and M. Cocco (2003), Slip-weakening behavior during the propagation of dynamic ruptures obeying rate- and state-dependent friction laws, *J. Geophys. Res.*, 108, No. B8, 2373, doi: 10.1029/2002JB002198, ESE 3-1-ESE 3-21.

Bizzarri, A., and M. Cocco (2005), 3D dynamic simulations of spontaneous rupture propagation governed by different constitutive laws with rake rotation allowed, *Annals of Geophysics*, 48, No. 2, 279-299.

Bizzarri, A., and M. Cocco (2006a), A thermal pressurization model for the spontaneous dynamic rupture propagation on a three-dimensional fault: 1. Methodological approach, *J. Geophys. Res.*, 111, B05303, doi: 10.1029/2005JB003862.

Bizzarri, A., and M. Cocco (2006b), A thermal pressurization model for the spontaneous dynamic rupture propagation on a three-dimensional fault: 2. Traction evolution and dynamic parameters, *J. Geophys. Res.*, 111, B05304, doi: 10.1029/2005JB003864.

Bizzarri, A. and M. Cocco (2006c), Comment on "Earthquake cycles and physical modeling of the process leading up to a large earthquake", *Earth Planets Space*, 58, 1525-1528.

Bizzarri, A., Cocco M., Andrews D. J., and E. Boschi (2001), Solving the dynamic rupture problem with different numerical approaches and constitutive laws, *Geophys. J. Int.*, 144, 656-678.

Boatwright, J., and M. Cocco (1996), Frictional constraints on crustal faulting, *J. Geophys. Res.*, 101, No. B6, 13,895-13,909.

Bouchon, M. (1981), A simple method to calculate Green's function for layered media, *Bull. Sesim. Soc. Am.*, 71, 959-971.

Brodsky, E. E., V. Karakostas, and H. Kanamori (2000), A new observation of dynamically triggered regional seismicity: Earthquakes in Greece following the August 1999 Izmit, Turkey earthquake, *Geophys. Res. Lett.*, 27, 2741-2744.

*Dynamic triggering in 3-D*

- 1  
2  
3  
4 Byerlee, J. (1990), Friction, overpressure and fault normal compression, *Geophys. Res. Lett.*, *17*,  
5  
6 2109–2112.  
7  
8  
9 Byerlee, J. (1993), Model for episodic flow of high–pressure water in fault zones before  
10  
11 earthquakes, *Geology*, *21*, 303–306.  
12  
13 Clifton, A. E., C. Pagli, J. F. Jonsdottir, K. Eythorsdottir, and K. Vogfjord (2003), Surface effects of  
14  
15 triggered fault slip on Reykjanes Peninsula, SW Iceland, *Tectonophys.*, *369*, No. 3–4, 145–154.  
16  
17 Cocco M., and A. Bizzarri (2002), On the slip–weakening behavior of rate– and state–dependent  
18  
19 constitutive laws, *Geophys. Res. Lett.*, *29*, No. 11, 11-1–11-4.  
20  
21  
22 Cotton, F., and M. Campillo (1994), Application of seismogram synthesis to the study of  
23  
24 earthquake source from strong motion records, *Ann. Geophys.*, *XXXVII*, No. 6, 1539–1564.  
25  
26  
27 Cotton, F., and O. Coutant (1997), Dynamic stress variations due to shear faults in a plane layered  
28  
29 medium, *Geophys. J. Int.*, *128*, 676–688.  
30  
31  
32 Crampin, S., T. Volti, S. Chastin, A. Gudmundsson, and R. Stefansson (2002), Indication of high  
33  
34 pore fluid pressures in a seismically–active fault zone, *Geophys. J. Int.*, *151*, F1– F5.  
35  
36  
37 de Boor, C. (1978), *A Practical Guide to Splines*, Springer–Verlag, New York.  
38  
39  
40 Dziewonski, A. M., T. A. Chou, and J. H. Woodhouse (1981), Determination of earthquake source  
41  
42 parameters from waveform data for studies of global and regional seismicity, *J. Geophys. Res.*,  
43  
44 *86*, 2825–2852.  
45  
46  
47 Eberhart–Phillips, D. et al. (2003), The 2002 Denali Fault Earthquake, Alaska: A large magnitude,  
48  
49 slip–partitioned event, *Science*, *300*, 1113–1118.  
50  
51  
52 Gomberg, J. (2001), The failure of the earthquake failure models, *J. Geophys. Res.*, *106*, 16,253–  
53  
54 16,263.  
55  
56  
57 Gomberg J., P. A. Resenberg, P. Bodin, and R. A. Harris (2001), Earthquake triggering by seismic  
58  
59 waves following the Landers and Hector Mine earthquake, *Nature*, *411*, 462–466.  
60  
Haar, L., J. S. Gallagher, and G. S. Kell (1984), NBS/NRC Steam Tables, Hemisphere Publ. Co.,

1  
2  
3  
4 NY.

5  
6 Hersir, G. P., A. Bjornsson, and L. B. Pedersen (1984), Magnetotelluric survey across the active  
7 spreading zone in southwest Iceland, *J. Volcanology and Geothermal Res.*, 20, 253–265.

8  
9 Hjaltdottir, S., and K. S. Vogfjord (2005), Subsurface fault mapping in Southwest Iceland by  
10 relative location of aftershocks of the June 2000 earthquakes, *Report Rit Vedurstofu Icelanda*,  
11 21, VI–ES–01, Reykjavik.

12  
13 Hubbert, M. K., and W. W. Rubey (1959), Mechanics of fluid-filled porous solids and its  
14 application to overthrust faulting, *Bull. Geol. Soc. Am.*, 70, 115–166.

15  
16 Hunt, J. M. (1990), Generation and migration of petroleum from abnormally pressurized fluid  
17 compartments, *Am. Asso. Petrol. Geol. Bull.*, 74, 1–12.

18  
19 Ida, Y. (1972), Cohesive force across the tip of a longitudinal–shear crack and Griffith's specific  
20 surface energy, *J. Geophys. Res.*, 77, No. 20, 3796–3805.

21  
22 Kanamori, H. (1977), The energy release in great earthquakes, *J. Geophys. Res.*, 82, 2981–2987.

23  
24 King, G. C. P., R. S. Stein, and J. Lin (1994), Static stress changes and the triggering of  
25 earthquakes, *Bull. Seism. Soc. Am.*, 84, No. 3, 935–953.

26  
27 Linker, M. F., and J. H. Dieterich (1992), Effects of variable normal stress on rock friction:  
28 observations and constitutive equations, *J. Geophys. Res.*, 97, No. B4, 4923–4940.

29  
30 Miller, S. A., A. Nur, and D. L. Olgaard (1996), Earthquakes as a coupled shear stress–high pore  
31 pressure dynamical system, *Geophys. Res. Lett.*, 23, 197–200.

32  
33 Ohnaka, M. (2003), A constitutive scaling law and a unified comprehension for frictional slip  
34 failure, shear fracture of intact rocks, and earthquake rupture, *J. Geophys. Res.*, 108, N. B2,  
35 2080, doi: 10.1029/2000JB000123.

36  
37 Ohnaka, M., Y. Kuwahara, and K. Yamamoto (1987), Constitutive relations between dynamic  
38 physical parameters near a tip of the propagating slip zone during stick–slip shear failure,  
39 *Tectonophysics*, 144, 109–125.

40  
41 Ohnaka, M., and T. Yamashita (1989), A cohesive zone model for dynamic shear faulting based on  
42  
43  
44  
45  
46  
47  
48  
49  
50  
51  
52  
53  
54  
55  
56  
57  
58  
59  
60



*Dynamic triggering in 3-D*

- 1  
2  
3  
4 experimentally inferred constitutive relation and strong motion source parameters, *J. Geophys.*  
5  
6 *Res.*, 94, No. B4, pp. 4089–4104.  
7  
8  
9 Pedersen, R., F. Sigmundsson, K. L. Feigl, and T. Arnadóttir (2001), Coseismic interferograms of  
10  
11 two  $M_s = 6.6$  earthquakes in the South Iceland Seismic Zone, June 2000, *Geophys. Res. Lett.*,  
12  
13 28, No. 17, 3341–3344.  
14  
15  
16 Peyrat, S., K. B. Olsen., and R. Madariaga (2001), Dynamic modeling of the 1992 Landers  
17  
18 earthquake, *J. Geophys. Res.*, 106, No. B11, 26,467–26,482.  
19  
20  
21 Powley, D. E. (1990), Pressures and hydrogeology in petroleum basins, *Earth Sci. Rev.*, 29, 215–  
22  
23 226.  
24  
25  
26 Rice, J. R. (1992), Fault stress states, pore pressure distributions, and the weakness of the San  
27  
28 Andreas Fault, in *Fault Mechanics and Transport Properties in Rocks (the Brace Volume)*,  
29  
30 Edited by B. Evans and T.–F. Wong, Academic, San Diego, 475–503.  
31  
32  
33 Ripperger, J., and P. M. Mai (2004), Fast computation of static stress changes on 2D faults from  
34  
35 final slip distributions, *Geophys. Res. Lett.*, 31, L18610, doi: 10.1029/2004GL020594.  
36  
37  
38 Rubin, A. M., and J.–P. Ampuero (2005), Earthquake nucleation on (aging) rate and state faults, *J.*  
39  
40 *Geophys. Res.*, 110, B11312, doi: 10.1029/2005JB003686.  
41  
42  
43 Ruina, A. L. (1983), Slip instability and state variable friction laws, *J. Geophys. Res.*, 88, No. B12,  
44  
45 10,359–10,370.  
46  
47  
48 Scholz, C. H. (2002), The mechanics of earthquakes and faulting, 2<sup>nd</sup> edition, *Cambridge University*  
49  
50 *Press*, Cambridge.  
51  
52 Stark, M. A., and S. D. Davis (1996), Remotely triggered microearthquakes at the Geysers  
53  
54 geothermal field, California, *Geophys. Res. Lett.*, 23, 945–948.  
55  
56  
57 Stefansson, R., G. Gudmundsson, and P. Haldórsson (2003), The South Iceland earthquakes 2000 a  
58  
59 challenge for earthquake prediction research, URL:  
60 <http://hraun.vedur.is/ja/prepared/SouthIcelandEarthq2000/>, last modified April 2, 2003.

- 1  
2  
3  
4 Vogfjord, K. S., G. Nolet, W. J. Morgan, R. Allen, R. Slunga, B. Bergsson, P. Erlendsson, G.  
5  
6 Foulger, S. Jakobsdottir, B. Julian, M. Pritchard, S. Ragnarsson, and R. Stefansson (2002),  
7  
8 Crustal profiling in Iceland using earthquake source arrays, *EOS. Trans. AGU*, 83(45), Fall  
9  
10 Meet. Suppl., Abstract S61C 1161.  
11  
12  
13 Vogfjord, K. (2003), Triggered seismicity after the June 17,  $M_w=6.5$  earthquake in the South  
14  
15 Iceland Seismic Zone: the first five minutes, *Geophys. Res. Abstracts*, 5, 11251.  
16  
17  
18 Voisin, C. (2002), Dynamic triggering of earthquakes: the nonlinear slip-dependent friction case, *J.*  
19  
20 *Geophys. Res.*, 107, B12, 2356, doi: 10.1029/2001JB001121.  
21  
22  
23 Voisin, C., M. Campillo, I. Ionescu, F. Cotton, and O. Scotti (2000), Dynamic versus static stress  
24  
25 triggering and friction parameters: Inferences from the November 23, 1980, Irpinia earthquake,  
26  
27 *J. Geophys. Res.*, 105, No. 9, 21,647–21,659.  
28  
29  
30 Voisin, C., F. Cotton, and S. Di Carli (2004), A unified model for dynamic and static stress  
31  
32 triggering of aftershocks, antishocks, remote seismicity, creep events, and multisegmented  
33  
34 rupture, *J. Geophys. Res.*, 109, B06304, doi: 10.1029/2003JB002886.  
35  
36  
37 Zencher, F., M. Bonafede, and R. Stefansson (2006), Near-lithostatic pore pressure at seismogenic  
38  
39 depths: a thermoporoelastic model, *Geophys. J. Int.*, 166, 1318–1334.  
40  
41  
42 Ziv, A. (2006), On the role of multiple interactions in remote aftershock triggering: the Landers and  
43  
44 the Hector Mine case studies, *Bull. Seism. Soc. Am.*, 96, 80–89.  
45  
46  
47  
48  
49  
50  
51  
52  
53  
54  
55  
56  
57  
58  
59  
60

Dynamic triggering in 3-D

## Figure Captions

**Figure 1.** Location of the two mainshocks (large stars) of June 17, 2000 (J17) and June 21, 2000 (J21) and aftershocks occurring within five minutes after the first mainshock (small stars) in the South Iceland Seismic Zone (SISZ). The 26 s event and 30 s event occurred in the Reykjanes Peninsula (RP) on the Hvalhnúkur fault (H) and Kleifarvatn fault (K), respectively. The epicenter of the 8 s event is represented by the small black star near the J17 fault. Light shaded areas are individual spreading segments with associated central volcanoes (He is the Hengill Volcano and Sv the geothermal area of Svartsengi). The Western Volcanic Zone (WVZ) and the Eastern Volcanic Zone (EVZ) are also indicated. After Arnadóttir et al. (2004).

**Figure 2.** (a) Coordinate systems used in this work:  $OX_1X_2X_3$  is the north–east–depth system with respect to which coordinates of the receivers are defined, while  $Ox_1x_2x_3$  is the local system. (b) Three–dimensional view of the local coordinate system: the vertical plane  $x_2 = x_2^f(\Sigma)$  represents the fault, while dashed lines represent the ends of the computational spatial domain  $\Omega^{(FD)}$ . Considering the spatial distribution of the change of the Coulomb Failure Function in the RP (see Figure 3 of AEA06) we have set the origin  $O$  of the  $Ox_1x_2x_3$  reference frame in order to have the epicenter of the 26 s event located at 16.5 km in the strike direction.  $\mathcal{T}^{(\hat{n})}$  is the total traction acting on  $\Sigma$ ,  $\mathbf{T}^{(\hat{n})}$  is its shear component and  $\mathbf{\Sigma}^{(\hat{n})}$  its normal component.

**Figure 3.** Distribution of the perturbed rupture times obtained for the test case A in Table 2. All model parameters are listed in Table 1, the initial effective normal stress is homogeneous on the whole fault plane and equal to 2.5 MPa and the Dieterich–Ruina governing law (equation (2)) is assumed. The black regions indicate where  $v < v_l$ . The two dashed grey lines identify the area  $\mathcal{I}$  that is expected to behave seismically (see Appendix C.1).

1  
2  
3  
4  
5  
6  
7  
8  
9  
10  
11  
12  
13  
14  
15  
16  
17  
18  
19  
20  
21  
22  
23  
24  
25  
26  
27  
28  
29  
30  
31  
32  
33  
34  
35  
36  
37  
38  
39  
40  
41  
42  
43  
44  
45  
46  
47  
48  
49  
50  
51  
52  
53  
54  
55  
56  
57  
58  
59  
60

**Figure 4.** (a) Initial pore fluid pressure profiles considered in this study; the solid gray line corresponds to equation (C.2), with  $x_3^* = 5800$  m,  $D^* = 3000$  m and  $h^* = 360$  m. (b) Initial effective normal stress profiles corresponding to the three profiles of  $p_{fluid}$  displayed in panel (a). The reference initial effective normal stress  $\sigma_n^{eff*}$  (vertical thin gray line) is superimposed for comparison.

**Figure 5.** (a) The same as in Figure 3, but now (case B in Table 2) the initial effective normal stress is variable along the depth as in profile #3 shown in Figure 4b (solid gray line). Snapshots of the fault slip velocity just before the triggered instability ( $t = 24.76$  s; panel (b)) and after  $t_p$ , at  $t = 25.08$  s (panel (c)) and at  $t = 25.40$  s (panel (d)). In all panels the dashed grey lines identify the area  $\mathcal{I}$  that is expected to behaves seismically (see Appendix C.1).

**Figure 6.** Perturbed failure times for the case C in Table 4: parameters are the same as for Figure 5, but now the parameter  $a$  is 0.012 for  $x_1 < 9700$  m and  $x_1 > 16500$  m. Notice that in order to emphasize the cracked area we report only a portion of the whole fault plane.

**Figure 7.** Comparison of the solutions in H from the 3–D fault model corresponding to Figure 5 (black solid squares; 3–D) and a spring–slider model (grey open circles; SS). (a) Fault slip velocity time history. (b) Particular of the fault slip velocity time history in a shorter time window. (c) Slip–weakening curve; the grey star denotes the state of the system when  $v = 0.1$  m/s (at  $t = t_p$ ), while the two black open stars denote the points at which  $v = 0.01$  m/s and  $v = 0.05$  m/s. In the two slip–weakening curves, points with the same value of slip do not correspond to the same value of time. (d) Total loads (namely  $-\mathcal{L}_1^{(3-D)} = -f_{r_1} + \tau_0 - \Delta\sigma_{21}$  and

### Dynamic triggering in 3-D

$\mathcal{L}^{(SS)} = \tau_0 - \Delta\sigma_{21}; f_{r_1}$  is the strike component of the dynamic load, see Appendix B for details). If we subtract  $f_{r_1}$  from  $\mathcal{L}_1^{(3-D)}$  we obtain the thin grey line, coincident with  $\mathcal{L}^{(SS)}$ , as expected. In panels (a) to (b) and (d) vertical light grey dashed lines indicate the time of the peak in  $-\Delta\sigma_{21}$  ( $t = t_A = 24.10$  s), while vertical full lines denote the perturbed failure time for the 3-D model ( $t_p = 24.94$  s). The time interval between vertical full lines and vertical light grey dashed line is the time delay  $t_d$ . The black dashed line in panel (d) indicates the peak of  $-\mathcal{L}_1^{(3-D)}$  ( $t = 24.30$  s).

**Figure 8.** (a) The same as in Figure 6a, but in the case of Ruina–Dieterich model (equations (3); case D in Table 2). (b) Fault slip velocity time history in H. (c) Detail of the fault slip velocity time history in a shorter time window. (d) Slip–weakening curve. Black solid squares refer to the 3-D model, while grey open circles to the spring–slider model. In panels (b) and (c) vertical light grey dashed lines indicate the time of the peak of  $-\Delta\sigma_{21}$  ( $t = t_A = 24.03$  s), while vertical full lines denote the perturbed failure times ( $t_p^{(3-D)} = 23.44$  s and  $t_p^{(SS)} = 23.93$  s). The grey star in panel (d) denotes the point in the slip–weakening curve corresponding to the perturbed failure time.

**Figure 9.** (a) The same as in Figure 5a, but assuming the non–linear slip–weakening constitutive model (equation (4); case E in Table 2). To help the comparison, we plot rupture times up to the maximum value of Figures 5a and 6. (b) Time snapshot of the fault slip velocity at  $t = 27$  s.

**Figure 10.** The same as in Figure 5a, but assuming a translated form of the Bouchon ramp source time function (case F in Table 2).

1  
2  
3  
4 **Figure A.1.** Distribution on the 26 s fault of the shear stress perturbations (namely  $\Delta\sigma_{21}(x_1, x_3, t)$ )  
5  
6 caused by the June 17 mainshock. Panels in the left column are the original values calculated in  
7 the 96 receivers, while panels in the right column are the interpolated values in the 42,471 fault  
8 points (see Appendix A for the details of the spatio-temporal interpolation algorithm). Panels  
9 (a) and (b) are at time  $t = 13.18$  s, panels (c) and (d) at time  $t = 26.37$  s. The black star is the  
10 observed hypocenter of the 26 s event.  
11  
12  
13  
14  
15  
16  
17  
18  
19

20 **Figure A.2.** Comparison between the original time series (black curves) and the interpolated time  
21 series (red curves) for the perturbation of shear stress (panel (a)) and normal stress (panel (b)),  
22 namely  $-\Delta\sigma_{21}(x_1, x_3, t)$  and  $\Delta\sigma_{22}(x_1, x_3, t)$ , respectively, in the hypocenter of the 26 s aftershock.  
23  
24  
25  
26  
27  
28  
29  
30  
31  
32  
33  
34  
35  
36  
37  
38  
39  
40  
41  
42  
43  
44  
45  
46  
47  
48  
49  
50  
51  
52  
53  
54  
55  
56  
57  
58  
59  
60

## Dynamic triggering in 3-D

## Tables

**Table 1.** Model discretization and constitutive parameters.

Parameter	Value
$\Omega^{(FD)}$	box that extends up to $x_{1_{end}} = 36.5$ km along $x_1$ , up to $x_{2_{end}} = 10$ km along $x_2$ and up to $x_{3_{end}} = 11.6$ km along $x_3$ (a)
$\Sigma$	$\{ \mathbf{x} \mid x_2 = x_2^f = 5 \text{ km} \}$
$\Delta x_1 = \Delta x_2 = \Delta x_3 \equiv \Delta x$	100 m (b)
Number of nodes	4,289,571
$\Delta t$	$1.27 \times 10^{-3}$ s (b)
Number of time levels	33,650
$v_l$	0.1 m/s
$\varphi(x_1, x_3, 0)$	$\varphi_0 = 180^\circ$
$v(x_1, x_3, 0)$	$v_{init} = 6.34 \times 10^{-10}$ m/s (= 20 mm/yr)
$\Psi(x_1, x_3, 0)$	$\Psi^{ss}(v_{init}) = 1.577 \times 10^6$ s ( $\cong 18.25$ d)
$\sigma_n^{eff*}$	2.5 MPa
$a$	0.003 (c)
$b$	0.010
$L$	$1 \times 10^{-3}$ m
$\mu_*$	0.7
$v_*$	$v_{init}$
$\alpha_{LD}$	0 (d)

(a) The boundaries of  $\Omega^{(FD)}$  are chosen such that radiation reflected by, or interacting with, the domain boundaries

does not pollute our results in the time window here considered.

(b) See Appendix A for details about the spatio-temporal discretization.

(c) In numerical experiments with heterogeneous rheology (see section 3.3) this is the value in the region  $9700 \text{ m} \leq x_1 \leq 16500 \text{ m}$ .

(d) We set  $\alpha_{LD} = 0$  in because the effect of the inclusion of the dependence on effective normal stress in the evolution equation for the state variable is negligible for instantaneous triggering and it plays an important role only in cases of delayed triggering (see AEA06 for a discussion). In this way the temporal variations of the effective normal stress influence the fault traction only through the explicit dependence of  $\tau$  on  $\sigma_n^{eff}$ .

**Table 2.** Synoptic list of the selected ensemble of numerical models discussed in this paper. DR stands for Dieterich–Ruina governing law (equation (2)), RD for Ruina–Dieterich (equation (3)), OY for Ohnaka–Yamashita slip–weakening (equation (4)). The initial effective normal stress is assumed to vary with depth as for profile #3 in Figure 4b, unless otherwise specified.

<i>Case</i>	<i>Constitutive law</i>	<i>Heterogeneous rheology</i>	<i>Hypocenter location</i> <sup>(a)</sup> (m)	<i>Origin time</i> <sup>(a)</sup> (s)	<i>Total seismic moment</i> $M_0$ (Nm)	<i>Figure</i>
A <sup>(c)</sup>	DR	No	(16500,2900)	23.47	$2.23 \times 10^{19}$	3
B	DR	No	(13200,7500)	24.94	$6.43 \times 10^{16}$	5, 7
C	DR	Yes	(13200,7500)	24.94	$2.27 \times 10^{16}$	6
D	RD	Yes	(15700,7900)	23.44	$2.02 \times 10^{16}$	8
E	OY	No	(22500,7700)	23.70	$2.49 \times 10^{19}$	9
F <sup>(c)</sup>	DR	No	(13200,7500)	26.42	$5.25 \times 10^{16}$	10
<i>Observational constraints</i>			<b>(16500 ± 450, 8900 ± 1300)</b>	<b>25.9 ± 0.1</b>	<b>[3.2×10<sup>16</sup>, 1.8×10<sup>17</sup>]</b>	<b>N/A</b>

<sup>(a)</sup> In case of model results, we indicate as hypocenter the “virtual” hypocenter H and as origin time the least perturbed failure time (see section 2.2). All times are referred to the June 17, 2000 mainshock origin time.

<sup>(b)</sup> In this case is:  $\sigma_{n_0}^{eff} = \sigma_n^{eff*}$ .

<sup>(c)</sup> The source time function is a translated from of the original ramp function (see section 7 for details), having the same characteristic time.

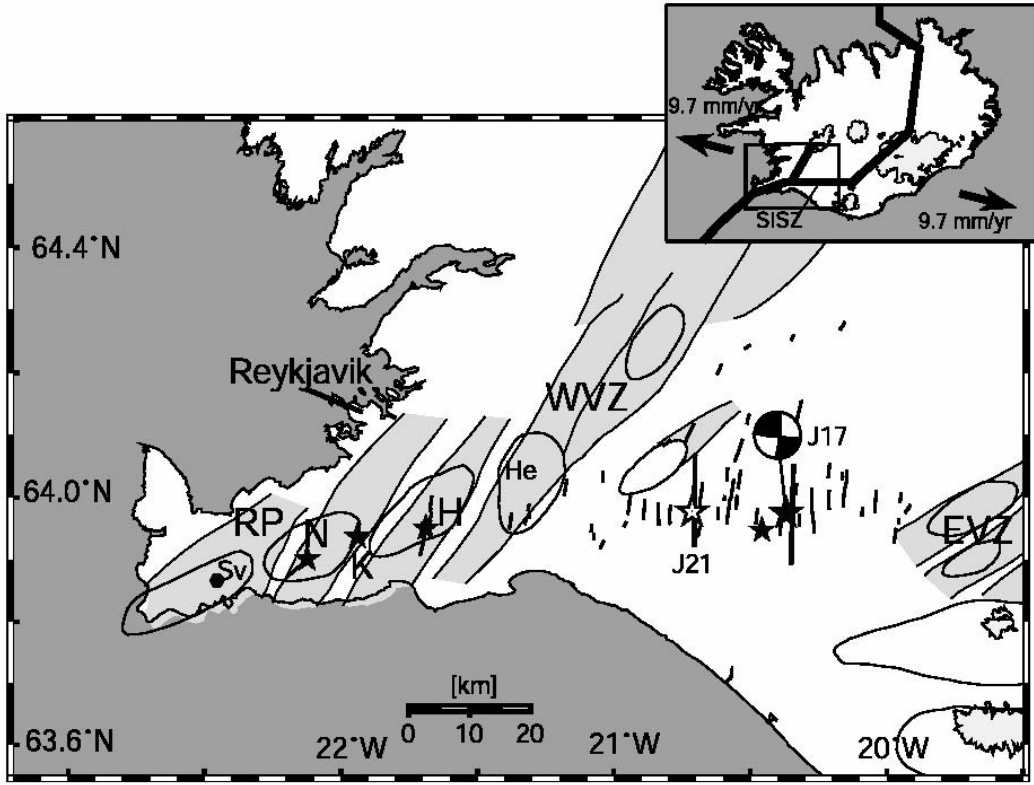


## Dynamic triggering in 3-D

**Table B.1.** Temperature and pore fluid pressure distributions on the fault plane (see Appendix C.2 for details).

<b>Layer # k</b>	<b>Overpressure <math>(\hat{p}^{(litho)} - p_{fluid}^{(hydro)})_k</math> (MPa)</b>	<b>Temperature <math>T_k^f</math> (°C)</b>	<b>Fluid density <math>\rho_{fluid,k}</math> (kg/m<sup>3</sup>)</b>	<b>Depth of <math>x_{3k}</math> (m)</b>
1	0.10	5.00	999.99	0
2	18.8	95.0	970.46	1000
3	38.1	185	914.40	2000
4	58.7	275	818.45	3000
5	82.0	365	716.70	4000
6	107	455	633.05	5000
7	134	545	541.20	6000
8	162	635	485.50	7000
9	190	725	465.30	8000
10	215	745	491.50	9000

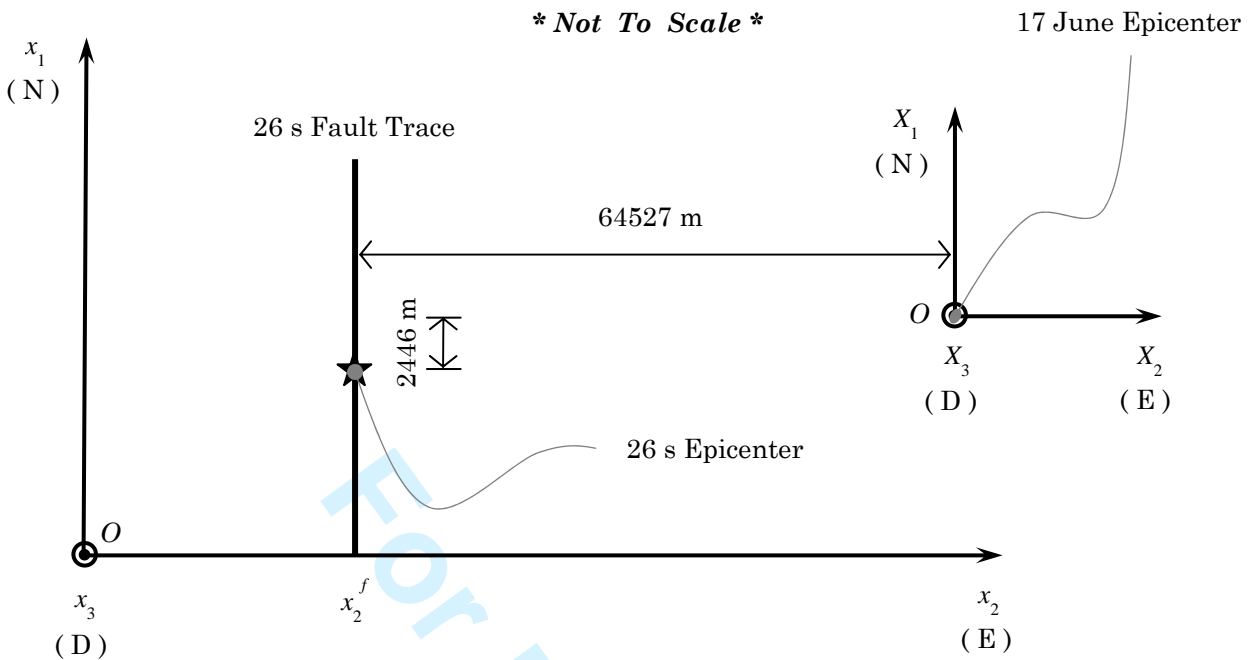
Figure 1



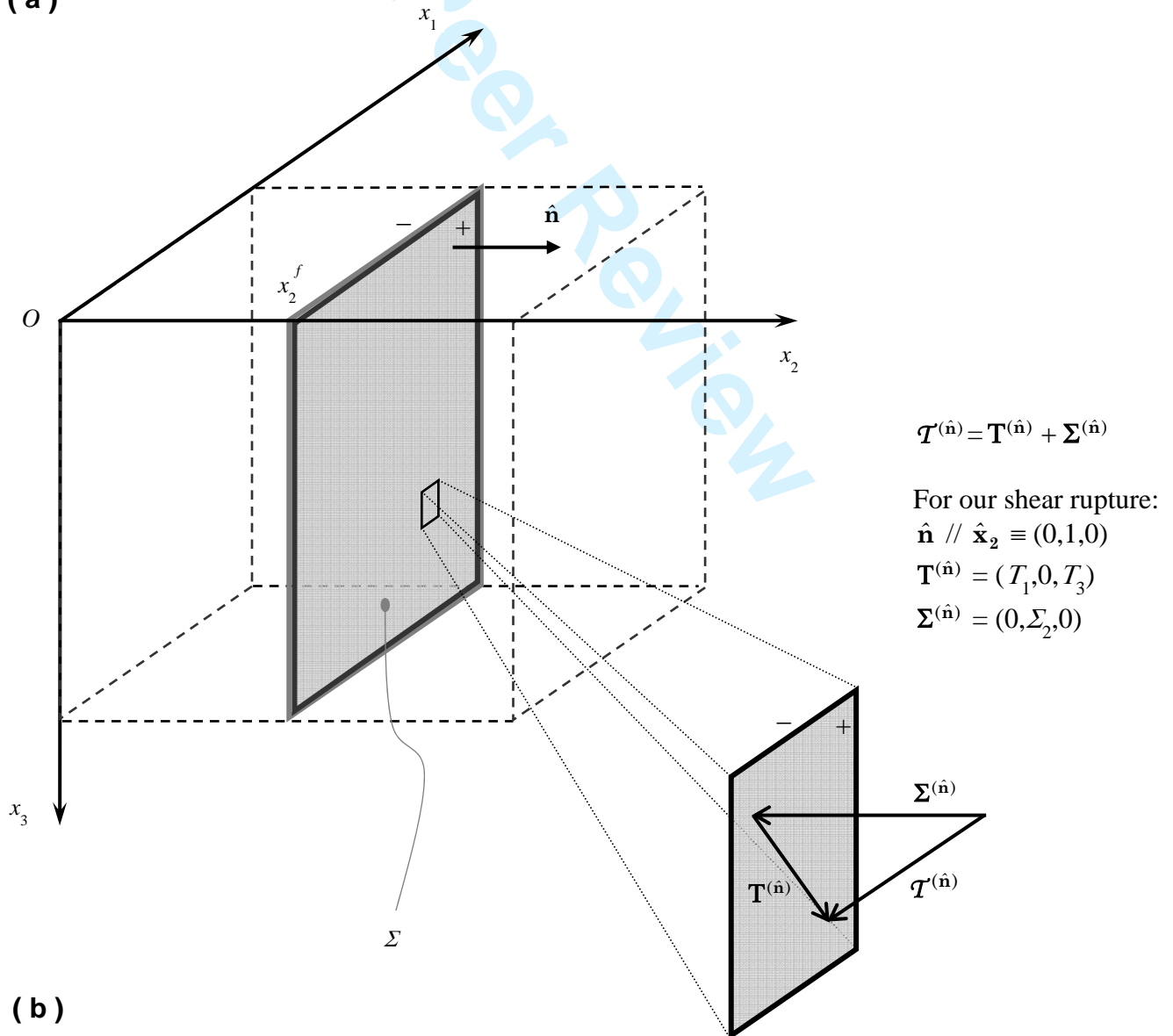
Review

1  
2  
3  
4  
5  
6  
7  
8  
9  
10  
11  
12  
13  
14  
15  
16  
17  
18  
19  
20  
21  
22  
23  
24  
25  
26  
27  
28  
29  
30  
31  
32  
33  
34  
35  
36  
37  
38  
39  
40  
41  
42  
43  
44  
45  
46  
47  
48  
49  
50  
51  
52  
53  
54  
55  
56  
57  
58  
59  
60

Figure 2



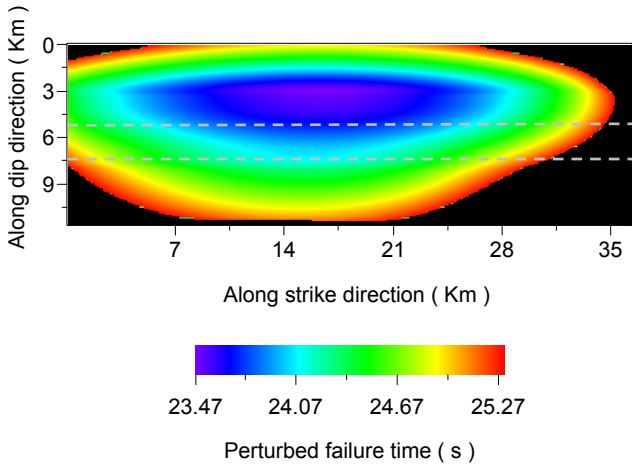
(a)



(b)

1  
2  
3  
4  
5  
6  
7  
8  
9  
10  
11  
12  
13  
14  
15  
16  
17  
18  
19  
20  
21  
22  
23  
24  
25  
26  
27  
28  
29  
30  
31  
32  
33  
34  
35  
36  
37  
38  
39  
40  
41  
42  
43  
44  
45  
46  
47  
48  
49  
50  
51  
52  
53  
54  
55  
56  
57  
58  
59  
60

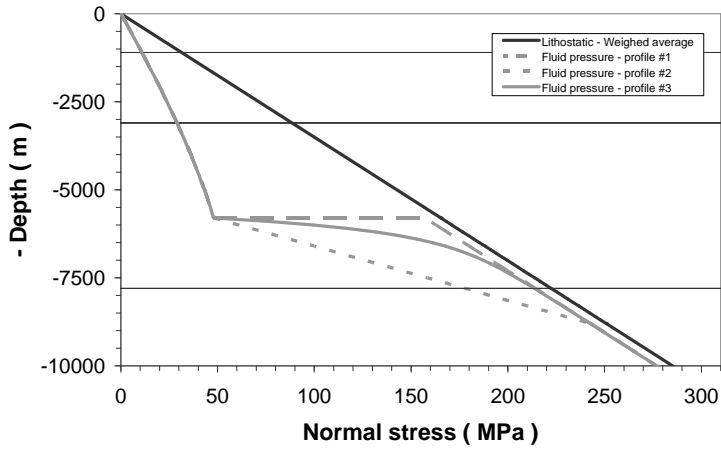
Figure 3



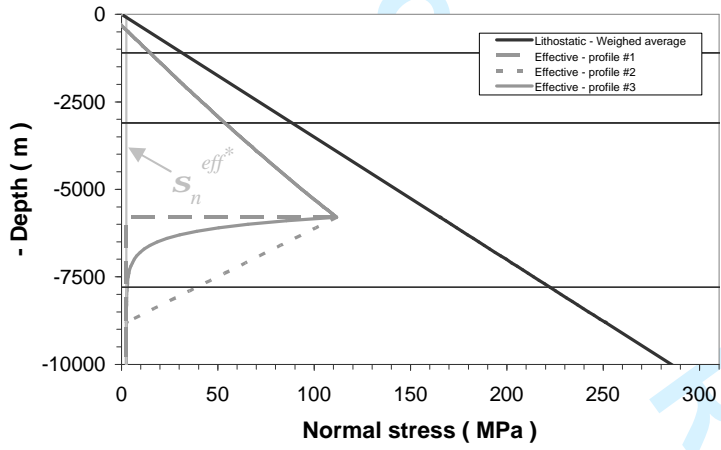
For Peer Review

1  
2  
3  
4  
5  
6  
7  
8  
9  
10  
11  
12  
13  
14  
15  
16  
17  
18  
19  
20  
21  
22  
23  
24  
25  
26  
27  
28  
29  
30  
31  
32  
33  
34  
35  
36  
37  
38  
39  
40  
41  
42  
43  
44  
45  
46  
47  
48  
49  
50  
51  
52  
53  
54  
55  
56  
57  
58  
59  
60

Figure 4



(a)



(b)

1  
2  
3  
4  
5  
6  
7  
8  
9  
10  
11  
12  
13  
14  
15  
16  
17  
18  
19  
20  
21  
22  
23  
24  
25  
26  
27  
28  
29  
30  
31  
32  
33  
34  
35  
36  
37  
38  
39  
40  
41  
42  
43  
44  
45  
46  
47  
48  
49  
50  
51  
52  
53  
54  
55  
56  
57  
58  
59  
60

Figure 5

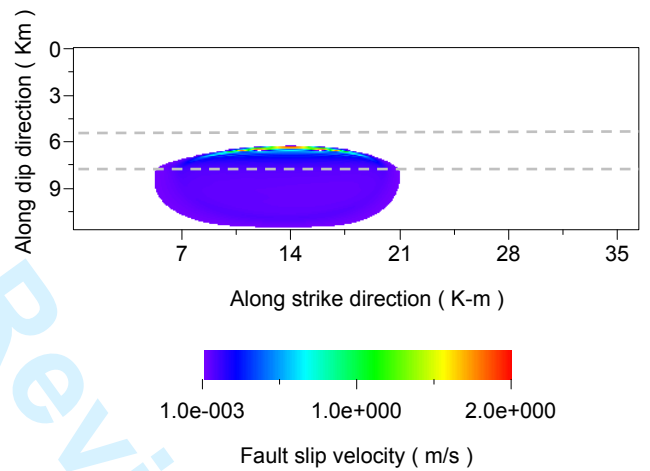
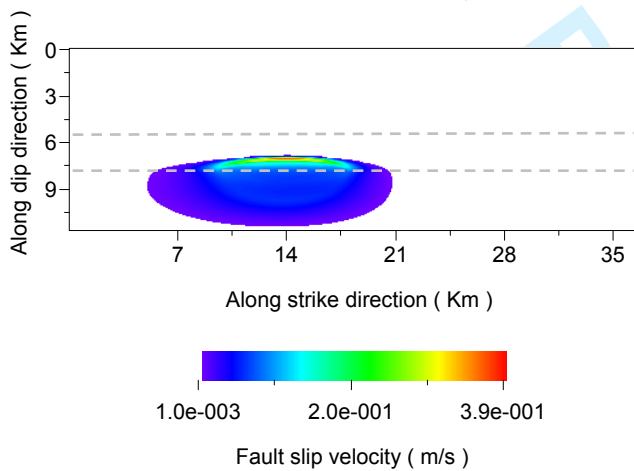
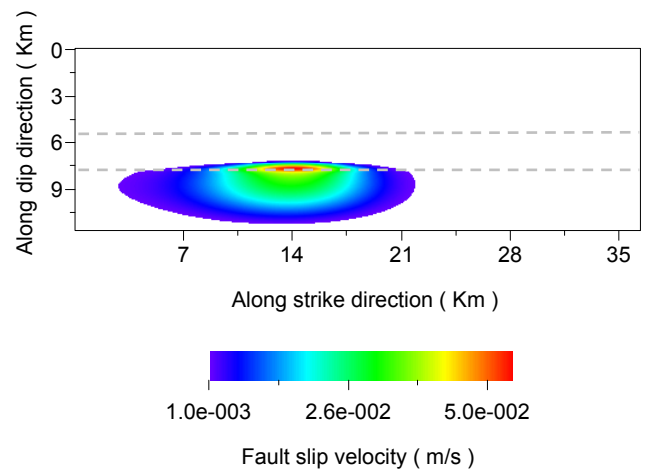
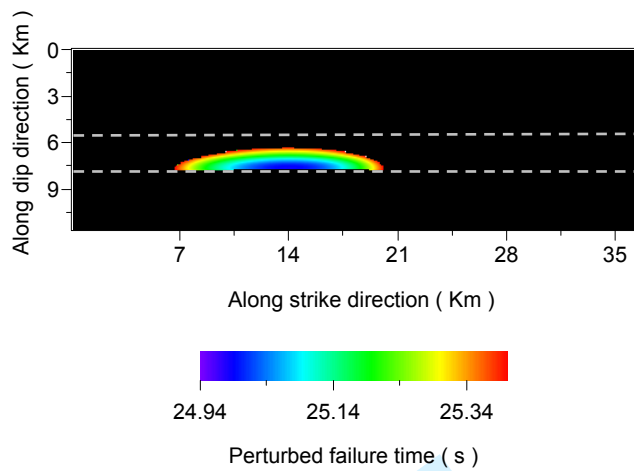
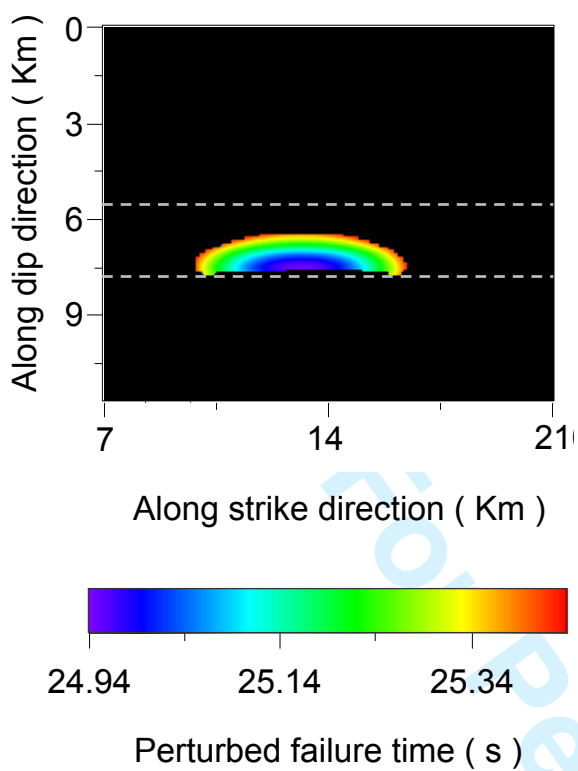


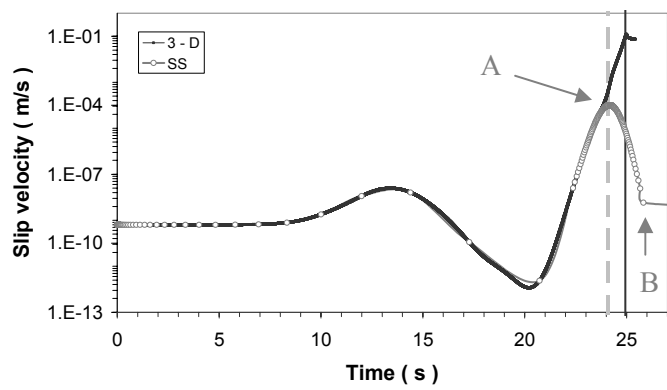
Figure 6



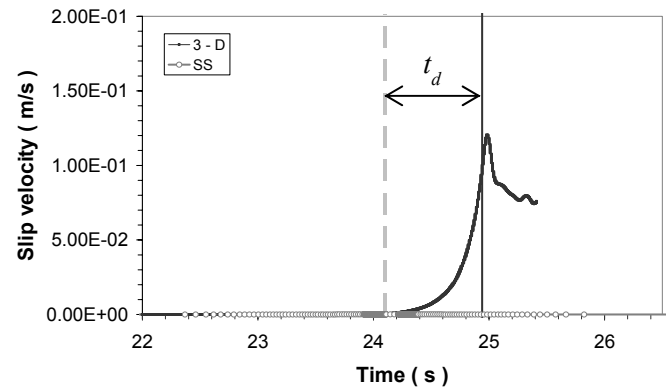
1  
2  
3  
4  
5  
6  
7  
8  
9  
10  
11  
12  
13  
14  
15  
16  
17  
18  
19  
20  
21  
22  
23  
24  
25  
26  
27  
28  
29  
30  
31  
32  
33  
34  
35  
36  
37  
38  
39  
40  
41  
42  
43  
44  
45  
46  
47  
48  
49  
50  
51  
52  
53  
54  
55  
56  
57  
58  
59  
60

Peer Review

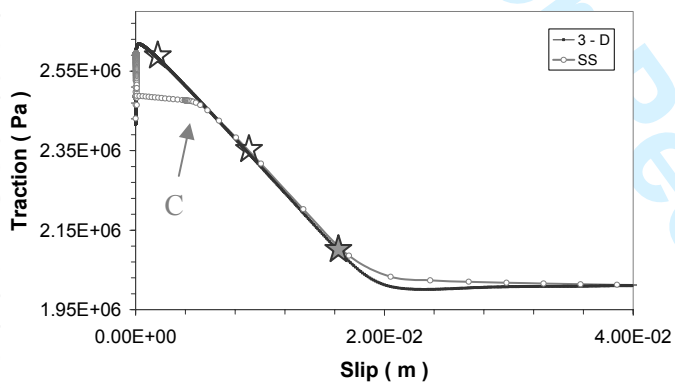
Figure 7



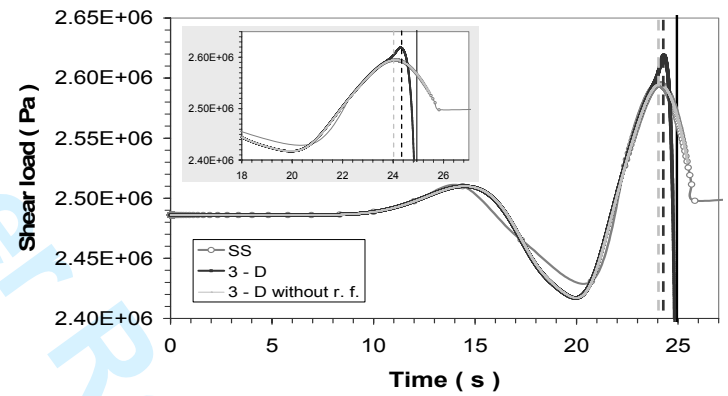
(a)



(b)



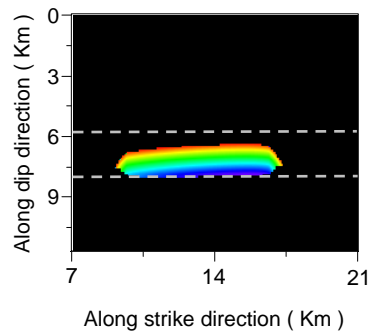
(c)



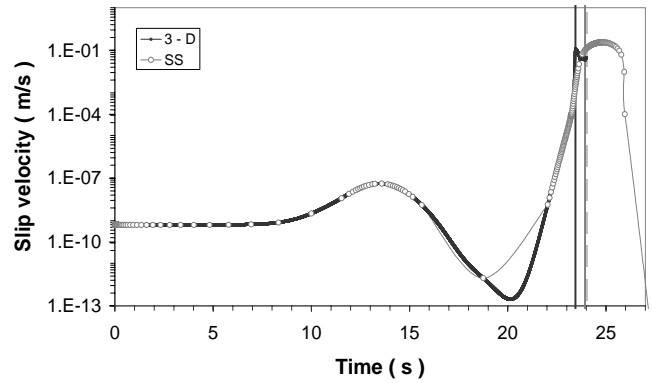
(d)



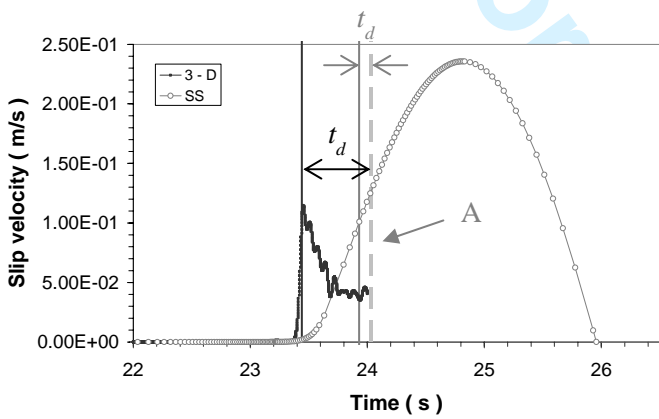
Figure 8



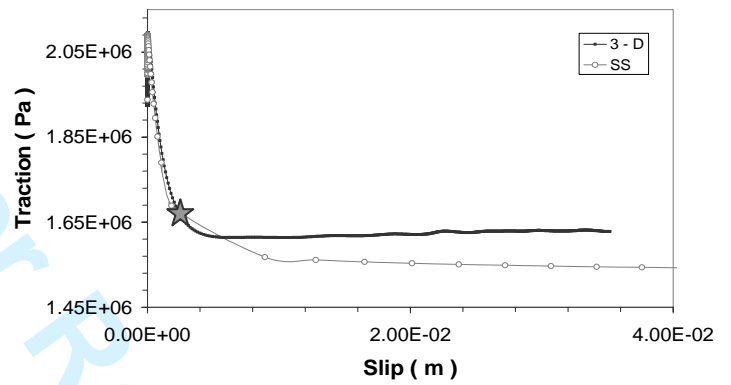
(a) 23.44 23.64 23.84  
Perturbed failure time ( s )



(b)

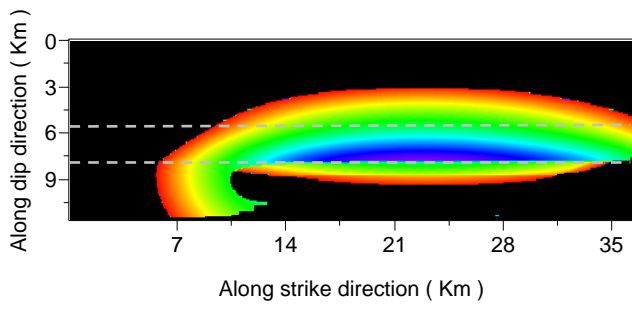
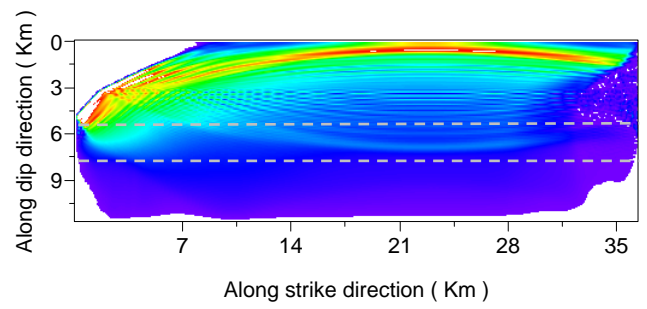


(c)



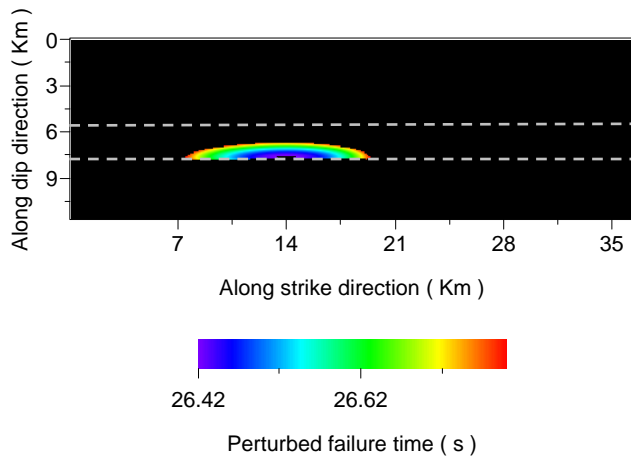
(d)

Figure 9

**(a)****(b)**

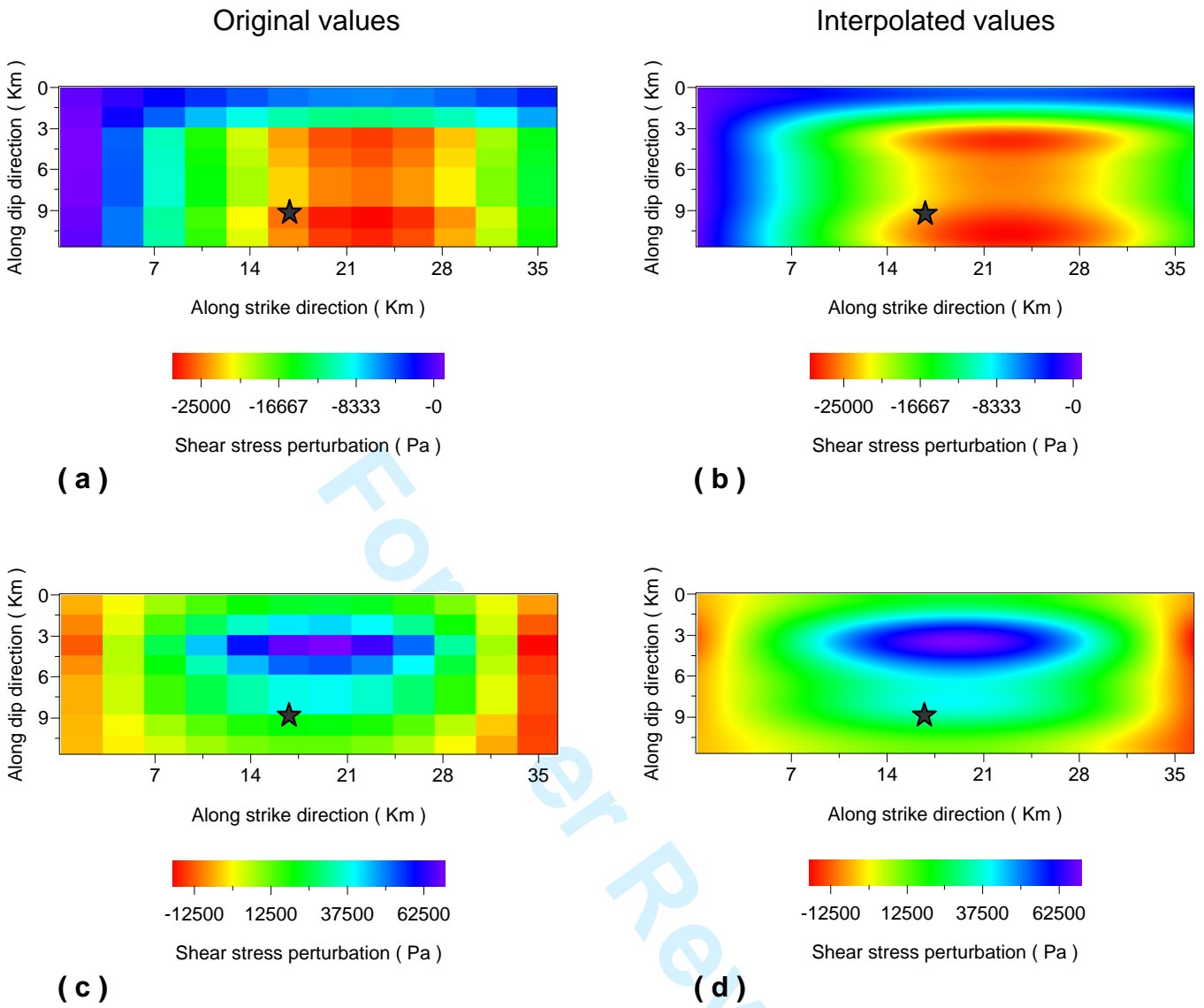
For Peer Review

Figure 10



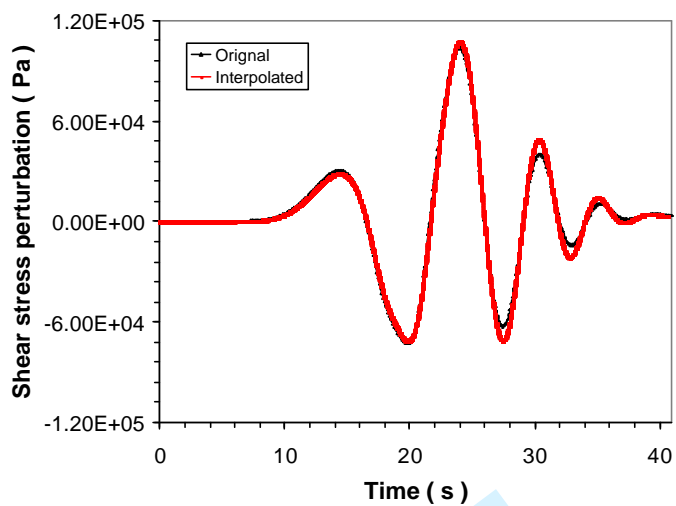
For Peer Review

Figure A.1

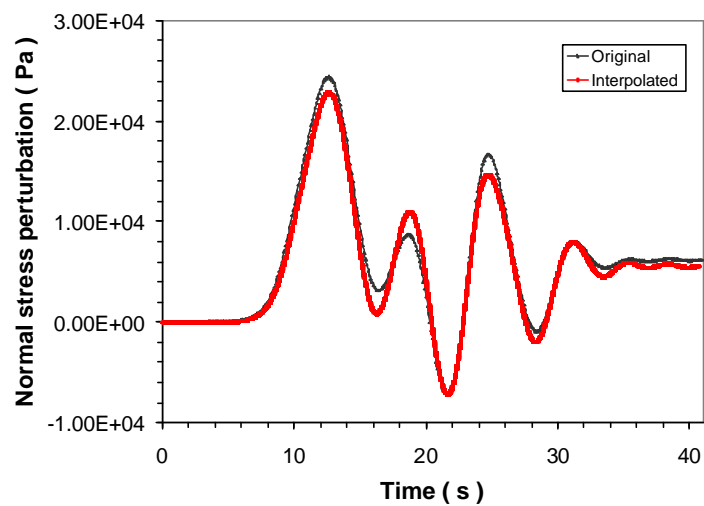


1  
2  
3  
4  
5  
6  
7  
8  
9  
10  
11  
12  
13  
14  
15  
16  
17  
18  
19  
20  
21  
22  
23  
24  
25  
26  
27  
28  
29  
30  
31  
32  
33  
34  
35  
36  
37  
38  
39  
40  
41  
42  
43  
44  
45  
46  
47  
48  
49  
50  
51  
52  
53  
54  
55  
56  
57  
58  
59  
60

Figure A.2



(a)



(b)

For Peer Review

*Dynamic triggering in 3-D – Auxiliary materials***Auxiliary material. Determination of the frictional parameter of the non-linear slip-weakening governing law (equation (4))**

From Figure 7c of the main text, in the “virtual” hypocenter we can estimate the following parameters: an upper yield strength  $\tau_u^{eq} = 2.62$  MPa, a frictional level  $\tau_f^{eq} = 2.01$  MPa, a hardening distance  $d_h = 3.31 \times 10^{-4}$  m and a slip-weakening parameter  $d_0^{eq} = 2.05 \times 10^{-2}$  m. The latter gives a ratio  $d_0^{eq}/L = 20.5$ , confirming also results obtained for a single fault with a homogeneous rheology (Cocco and Bizzarri, 2002, Bizzarri and Cocco, 2003). Considering that  $\tau_u^{eq} = \mu_u \sigma_n^{eff}$  and that  $\tau_f^{eq} = \mu_f \sigma_n^{eff}$  we obtain:  $\mu_u = 0.742$  and  $\mu_f = 0.569$ . In equation (4) we set  $d_0 = d_0^{eq}/5$  and, by definition, the parameters  $\alpha_{OY}$  and  $\beta_{OY}$  are determined by simultaneously solving the two transcendental equations:

$$\left\{ \begin{array}{l} \frac{d}{du} \tau \Big|_{u=d_h} = 0 \\ \tau(u=d_h) = \tau_u^{eq} \end{array} \right. \quad \begin{array}{l} \text{(AM.1)} \\ \text{(AM.2)} \end{array}$$

Numerical solutions of (AM.1) and (AM.2) are:  $\alpha_{OY} = 0.115634$  and  $\beta_{OY} = 1.31289 \times 10^{-5}$  m. The choice of  $d_0 = d_0^{eq}/5$  guarantees that the level of kinetic friction  $\tau_f^{eq}$  is reached when the cumulative slip is about  $2.05 \times 10^{-2}$  m (as in the case of DR law; see Figure 7c in the main text), nearly equal to  $12d_h$  (in agreement with laboratory observations of Ohnaka et al., 1987; their Figures 5a and 6a). We uniformly apply to all fault points the above-mentioned values for the constitutive parameters  $\alpha_{OY}$ ,  $\beta_{OY}$ ,  $d_0$  and  $\mu_f$ . On the contrary,  $\tau_0(x_1, x_3)$  has been set to be exactly equal to that used in cases B and C presented in the main text and therefore it is variable with depth.